DISCLAIMER

ORNL/TM-2025/4191

Parametric Optimization of Nanostructured Alumina-Forming Austenitic Alloys

Tim Graening
Caleb Massey
Holden Hyer
Yuki Yamamoto
David Collins
Thomas Siggillino
Marie Romedenne
Sebastien Dryepondt

September 2025

M3FT-25OR060101035

ORNL/TM-2025/4191

Innovative Nuclear Materials Program

PARAMETRIC OPTIMIZATION OF NANOSTRUCTURED ALUMINA-FORMING AUSTENITIC ALLOYS

Tim Graening
Caleb Massey
Holden Hyer
Yuki Yamamoto
David Collins
David Hoelzer
Thomas Siggillino
Marie Romedenne
Sebastien Dryepondt

September 2025

M3FT-25OR060101035

Prepared by
OAK RIDGE NATIONAL LABORATORY
Oak Ridge, TN 37831
managed by
UT-BATTELLE LLC
for the
US DEPARTMENT OF ENERGY
under contract DE-AC05-00OR22725

CONTENTS

LIST OF FIGURES

LIST OF TABLES

ACKNOWLEDGMENTS

This research was sponsored by the US Department of Energy Office of Nuclear Energy's Innovative Nuclear Materials Program under contract DE-AC05-00OR22725 with UT-Battelle LLC. One of the alloys analyzed in this work was originally developed under the Powertrain Materials Core Program, Vehicle Technologies Office, Office of Energy Efficiency and Renewable Energy. The authors thank Dr. Sam Bell and Dr. David Hoelzer for their thoughtful review of this report before publication. The authors would also like to thank Daniel Newberry and Jim Horenburg for their assistance with sample preparation. Finally, the research team would like to acknowledge Mr. Josh Kendall for operating the Renishaw, as well as the dedicated team of high-bay personnel (Kevin Hanson, Ryan Dalton, and Cody Taylor) for alloy extrusion services.

ABSTRACT

Alumina-forming austenitic (AFA) alloys provide excellent oxidation resistance through the formation of a stable alumina scale, but their relatively high Ni content might limit application in core structural components because of helium generation and swelling under irradiation. Increasing the density of nanoscale features in the microstructure is a promising route to improve sink strength and mitigate these effects. Conventional oxide dispersion–strengthened (ODS) steels achieve this through mechanical alloying (MA), but the approach is costly and difficult to scale. In this milestone, additive manufacturing was applied as an alternative pathway to fabricate nanostructured AFA (NAFA) alloys with dual precipitation of oxides and nitrides enabled by reactive atmosphere processing. In FY25, two compositions, NAFA-1 (AFA-05) and NAFA-2, were produced and compared. Both alloys achieved densities above 99% of theoretical values, but NAFA-2 exhibited microcracking associated with Nb-rich intermetallic formation, indicating the need for further chemistry optimization. Nitrogen and oxygen uptake was confirmed on selected builds, demonstrating the intended dual-precipitate dispersion. Mechanical testing showed that AM-processed NAFA alloys exceed conventionally produced ODS steels in high-temperature tensile strength and fracture toughness. Preliminary Cu ion irradiation results further suggest improved resistance compared to wrought austenitic alloys. While the current alloys are promising for their compatibility in high-temperature air or liquid Pb environments, modifications to composition will be required for long-term operation in high-temperature impure sodium systems. Future work will focus on refining alloy chemistry to suppress laser powder bed fusion–induced cracking and scaling production to reactor-relevant dimensions using directed energy deposition as a pathway toward net-shape cladding fabrication.

1. INTRODUCTION

Nuclear energy has a unique opportunity to serve as a safe, reliable, and constant source of energy for the projected surge in data center energy demand driving the artificial intelligence boom within the United States. Unfortunately, however, next-generation reactor vendors are struggling to qualify and deploy their reactor designs due to (1) the slow and arduous nuclear qualification process, and (2) the attempt to leverage century-old materials for reactors that are expected to deviate from historical experimental reactor operational envelopes. The Innovative Nuclear Materials (INM) program was created to help drive innovation in new cladding material candidates that can help improve operating envelopes for a wide array of advanced reactor technologies.

Candidate cladding and core structural materials for advanced reactor systems must combine high creep strength with exceptional resistance to irradiation-induced damage, while also withstanding aggressive coolant environments ranging from flowing lead, sodium, and supercritical CO_2, steam, and air at elevated temperatures (350–700°C). Alumina-forming austenitic (AFA) stainless steels represent one of the most mature alloy classes for such demanding service. These fully face-centered cubic (FCC) Fe-based alloys were originally developed in the early 2000s for fossil energy systems, where their high aluminum content promoted the formation of a protective alumina scale in place of the less stable chromium oxide films that form on traditional stainless steels [1].

However, conventional AFAs face important limitations when translated to reactor core conditions. First, their FCC structure will form stacking-fault tetrahedra, a specific type of irradiation-induced arrangement of defects under irradiation, which are known to be biased sinks that increase cavity swelling rates relative to alloys with ferritic body-centered cubic crystal structures [2]. In addition, their high nickel content is predicted to increase helium production through transmutation, raising concerns about helium-induced embrittlement at higher temperatures (>550°C) [3]. While the alloys inherently contain intermetallic and carbide precipitates, it is unclear whether these features alone provide sufficient sink strength to manage irradiation-driven defect populations, or whether additional precipitation due to radiation-enhanced segregation will significantly deteriorate high-temperature fracture toughness. Without improvement, AFAs in their wrought form may not fully meet the requirements for cladding or other in-core components.

One promising approach to overcome these shortcomings is to enhance the density of nanoscale point-defect sinks in the microstructure. Increasing the number of finely dispersed features—whether oxides, carbides, or nitrides—could improve recombination of point defects, stabilize helium bubbles, and mitigate high-temperature helium embrittlement. If realized, such improvements would make nanostructured AFAs (NAFAs) viable candidates for advanced fission reactor environments, extending their utility to lead-cooled fast reactors (LFRs) and microreactors without requiring additional barrier coatings.

This report focuses on the simultaneous evaluation of precipitation state and mechanical performance as a function of alloy processing conditions (namely, alloy composition and the use of reactive atmosphere). Subsequently, key performance metrics, such as the irradiation resistance and corrosion resistance, have been screened using accelerated screening experiments, including high-temperature sodium exposure and high-temperature ion-irradiation experiments.

2. MATERIALS AND METHODS

This section outlines the workflow pertaining to the process optimization conducted on the NAFA materials investigated in this work. First, fully dense samples of two different NAFA compositions were produced via printing in various reactive and inert atmospheres. Following specimen removal and machining, these specimens were subjected to different heat treatment, corrosive environments, irradiation fields, and/or high-temperature mechanical testing. These experiments were conducted to rapidly evaluate the suitability of the various NAFA compositions for environments expected specifically within sodium-cooled fast reactors (SFRs). A summary of this workflow is shown in Figure 1.

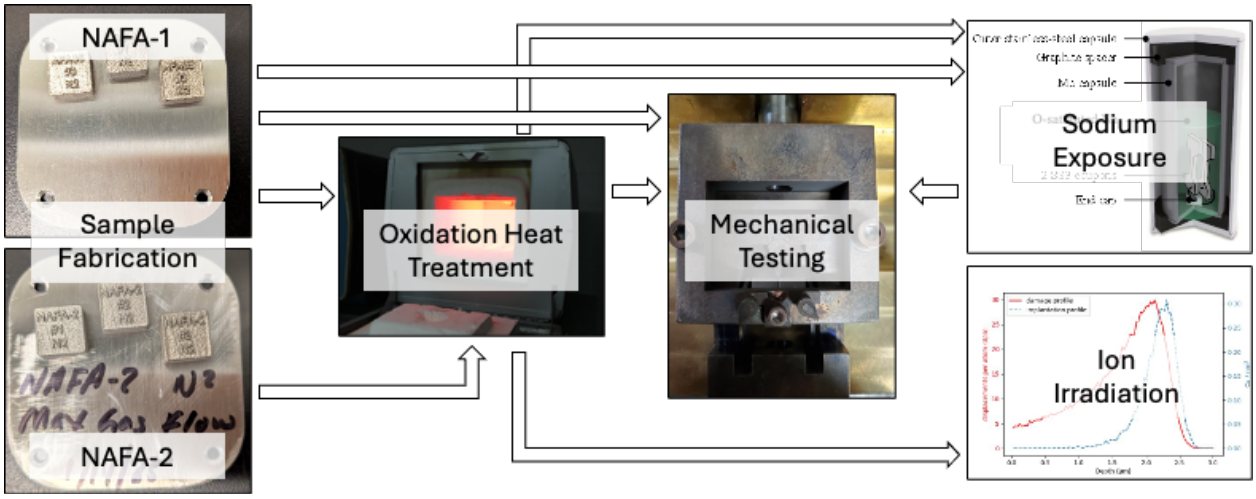

Figure 1. Workflow for sample preparation, post-build heat treatment, and environmental effects screening activities pursued in the current work.

2.1 MATERIAL SELECTION OF NOVEL NANOSTRUCTURED ALUMINA-FORMING AUSTENITIC STEEL

Additive manufacturing (AM) has emerged over the past decade as a disruptive alternative for producing oxide dispersion–strengthened (ODS) steels in a scalable and cost-effective manner [4]. Early studies showed that nano-oxide precipitates could, in principle, be generated through gas atomization reaction synthesis (GARS). Yet, those approaches consistently fell short: although nanoscale features formed, their number density rarely exceeded 10^{22} m^{-3}, remaining one to three orders of magnitude below what is routinely achieved in conventionally processed ODS steels [5-7]. Since nanoscale precipitates are essential for high-temperature creep strength and for defect recombination under irradiation, which is critical to mitigating high-temperature helium embrittlement [8-10], this posed a major limitation.

Our approach with NAFA was to rethink how those nanoscale features form. Instead of using oxygen present in the atmosphere to induce precipitation of oxides within the microstructure, the nitrogen and oxygen content was varied in the atmosphere to induce co-precipitation of both oxides and nitrides within the alloy microstructure. The idea is that dual precipitation (oxides + nitrides or carbide) could lift the total sink strength to levels closer to conventional ODS steels, while still taking advantage of AM scalability. Zirconium was added as an alloying element to stabilize nanoscale nitrides within the steel microstructure under AM conditions. At the same time, Nb content was increased to maximize Nb-rich carbide precipitation, to minimize uncontrolled carbide growth, and to improve oxidation resistance in air at 1000°C, which is critical for long-term creep life in air.

Processing was previously carried out under several processing atmospheres: pure Ar, a gas mixture (Ar +5 mol.% O_2 + 20 mol.% of N_2) ordered premixed from a supplier, and pure N_2 atmosphere. Here, NAFA was produced only via pure Ar (99.999%) and via pure N2 (99.999%) gases. At lower gas flow rates, separation occurs due to the different atomic masses: the heavier Ar atoms tend to remain closer to the printing surface inside the chamber, whereas the lighter N atoms are absent from the molten surface during the laser powder bed AM process. Oxygen was found to be sufficiently high as an impurity to form oxide precipitates in all samples. The resulting chemical composition analysis of printed samples regarding their oxygen and nitrogen content was performed and is reported in a later section.

Thermodynamic calculations were used to optimize NAFA composition by tuning alloying additions in Table 1 to reflect several targeted optimizations:

- **Chromium** to avoid sigma-phase formation
- **Carbon** to minimize $M_{23}C_6$ carbide precipitation
- **Nickel** to balance the reduced carbon levels and stabilize the FCC crystal structure
- **Molybdenum** as a solid-solution strengthener
- **Manganese** to further stabilize the FCC crystal structure
- **Tungsten** was completely removed, as it was not contributing positively under AM processing

These modifications to the alloy and the gas environment during the AM process mark a shift from the earlier GARS-based approach. Instead of relying on one mechanism to create sink strength, this design deliberately creates two different sink types, with oxides and nitrides forming independently but coexisting throughout the matrix. Two optimized alloy chemistries, NAFA-1 and NAFA-2, were manufactured using laser powder bed fusion (LPBF) in Ar or N_2 atmospheres. NAFA-1 and NAFA-2 compositions varied in terms of Cr, Ni, Nb, Mo, Zr and Y contents (Table 1). NAFA-1 was also previously conventionally produced via mechanical alloying (MA) [11].

Following manufacturing, room temperature tensile properties were measured. Compatibility was also investigated in static oxygen-saturated sodium at 700°C for 1,000 h and after Cu ion-irradiation.

Table 1. Specified chemical compositions of the novel NAFA-2 powder in comparison with the previous generation of NAFA-1. The compositions are in weight percent as provided in supplier material certifications.

	NAFA-1	NAFA-2
Element	Measured (wt.%)	Measured (wt%)
Fe	Bal.	Bal.
Cr	23.0	15.17
Mn	2.0	0.25
Ni	17.6	25.31
Cu	—	0.009
Al	4.0	3.58
Si	0.4	0.2
Nb	0.7	1.37
Mo	0.98	1.98
W	0.5	0.004
Zr	0.13	0.21
C	0.5	0.007
B	0.01	<0.001
N	0.04	0.029
Y	0.10	0.13

2.2 MATERIAL PRODUCTION VIA LASER POWDER BED FUSION

LPBF is an AM approach in which a laser selectively melts layers of powder, producing a consolidated component in a layer-by-layer fashion (Fig. 2). In this work, samples were produced using a Renishaw AM400 system that uses a pulsed laser scanned across a powder bed to melt and resolidify material into a fully dense part. The thermal input to the process can be tuned by adjusting several key parameters: laser power (p), scan velocity (v), hatch spacing between passes (h), and powder layer thickness (lt). These variables can be expressed collectively as a volumetric energy density (ED):

$$ED = \frac{p}{v \times h \times lt} \tag{1}$$

For pulsed-beam systems, like the one applied in this work, the laser does not move at a continuous speed but instead operates in an on/off mode while stepping between points. In this case, an effective scan velocity can be defined as

$$v = \frac{pd}{dt + t} \tag{2}$$

where pd is the point spacing, dt is the intrinsic laser dead time (10 μs in this system), and t is the programmed dwell time at each point. LPBF has been used as a first trial method, with more effort planned utilizing laser powder directed energy deposition (LP-DED) systems to optimize the powder flow and gas flow rates, with a combined lower cooling gradient to minimize cracking and optimize grain size and morphology.

The gas-atomized NAFA-1 and NAFA-2 powders were processed on a Renishaw AM400 laser powder bed fusion (LPBF) platform. The system is equipped with a Yb-fiber pulsed laser, with a nominal spot size of ~70 μm and a wavelength of 1.07 μm. Processing was structured around a design of experiments to systematically vary the primary laser parameters—laser power, dwell time, point spacing, and hatch spacing—in order to map the volumetric energy density window defined by Eq. (1). A constant powder layer thickness of 30 μm was used, based on prior experience with AFA alloys. A linear hatch vector scanning strategy was implemented, with each successive layer rotated by 67°. The stripe width between vector boundaries was fixed at 5 mm, and a hatch offset of 60 μm was applied to ensure overlap between adjacent passes. These parameters were chosen to reduce user bias by spanning a wide design space, while allowing quadratic regression of the results for identifying statistically significant effects. Experimental matrices were generated using Minitab (v.21) and used to guide all build trials. NAFA-1 was fabricated under both inert argon (99.999 mol%) and reactive nitrogen-rich (99.999 mol% N_2) atmospheres, while NAFA-2 was produced exclusively in an N_2 (99.999 mol%) atmosphere. The intent of these atmospheres was to promote the concurrent formation of oxides (via oxygen impurities in Ar and N2) and nitrides during solidification, creating the targeted dual-precipitate structure. Alloys were printed in simple cubic geometries (5 × 10 mm^2 cross-section, 12 mm height). The lower 2 mm was considered sacrificial and removed from the build plate by diamond wire saw, and the remaining material was used for characterization. Densities were measured by Archimedes immersion in ethanol at room temperature (~25°C) in accordance with ASTM B962, with three independent measurements performed for each specimen.

Archimedes testing confirmed that both NAFA-1 and NAFA-2 achieved high relative densities (>99% of theoretical) across a broad process window. NAFA-1 showed optimal densification near an energy density of ~131 J/mm^3 [3], while NAFA-2 reached peak density at somewhat lower input energies, suggesting a fundamental difference in processing response between the two alloys. Nitrogen-containing environments generally gave the most favorable results, though variations between atmospheres were within the uncertainty of the Archimedes method, as reported in a previous milestone report [11]. Statistical regression highlighted laser power and dwell time as the most critical parameters for densification, with point spacing also exerting a measurable influence through interaction effects. Cross-sectional analyses provided insight into the mechanisms driving density variations. Low energy input led to lack-of-fusion porosity with irregular pore shapes, while excessive energy caused keyholing and spherical gas porosity. The optimal regime (~70–131 J/mm^3 depending on material composition) minimized porosity and produced consistently dense material, and these parameters are summarized below in Table 2. However, even under these optimized conditions, microcracking was evident in NAFA-2 builds. These cracks, attributed to Nb-rich intermetallic formation during solidification, highlight a key limitation of the current chemistry. While density requirements can be met, the persistence of microcracking indicates that further alloy optimization is required.

This observation motivates the next stage of work, described in Section 2.4, which focuses on additional thermodynamic simulations and laboratory-scale fabrication of modified compositions. These efforts aim to resolve the solidification cracking issue in NAFA-2 by refining the chemistry while preserving the dual-precipitate strengthening concept.

Table 2. Density-optimized LPBF printing parameters for NAFA-1 and NAFA-2 builds analyzed in this work

Material Composition	NAFA-1	NAFA-2
Printing Unit	Renishaw AM250	Renishaw AM400
Layer Thickness (mm)	0.03	0.03
Stripe Width (µm)	5	5
Scan Rotation (degrees)	67	67
Hatch Offset (µm)	60	60
Delay Time (µs)	10	10
Laser Power (W)	200	150
Point Distance (µm)	60	70
Dwell Time (µs)	120	100
Hatch Spacing (mm)	0.11	0.11
Scan Speed (mm/s)	462	636
Energy Density (J/mm^3)	131	71
Spot Size (µm)	130	70

2.3 NAFA-2 OPTIMIZATION WORK

As NAFA-2 experienced microcracking during AM, efforts were made to identify the mechanism accelerating solidification cracking and to adjust the chemical composition to reduce the cracking behavior. The originally proposed NAFA-2 composition is shown in Table 3 with the ID AA241. Four variants of the material were produced to systematically investigate the impact of Cr, Nb, and Y on crack formation. The new compositions were manufactured using arc melting and the cracking susceptibility was investigated using autogenous gas tungsten arc welding (GTAW) to simulate LPBF processing, although the parameters are not directly comparable to LPBF. The parameters for GTAW were as follows: 150°C preheating, 100 A, 12 V, and a heat input of 236 J/mm to melt a single surface track.

Table 3. Chemical compositions of the NAFA-2 variants to assess solidification cracking susceptibility

ID	Alloy composition, wt.%											Remarks
	Fe	Cr	Mn	Ni	Al	Si	Nb	Mo	Zr	Y	C	
AA241	52	15	0.2	25	3.75	0.2	1.5	2	0.18	0.15	0.03	Many cracks in as-printed condition
AA242	52	15	0.2	25	3.75	0.2	1.5	2	0.18	0	0.03	Y-free
AA251	52	15	0.2	25	3.75	0.2	1.0	2	0.18	0	0.03	Low Nb for high T_m
AA252	50	17	0.2	25	3.75	0.2	1.0	2	0.18	0	0.03	High Cr for oxidation resistance, low Nb for high T_m
AA253	51	17	0.2	25	3.75	0.2	0.8	2	0.18	0	0.03	High Cr for oxidation resistance, lower Nb for higher T_m

2.4 MICROSCOPY METHODS

The alloy microstructures were examined using a combination of scanning electron microscopy (SEM) and transmission electron microscopy (TEM). SEM imaging and EBSD maps were carried out on a TESCAN MIRA3 system fitted with an Oxford Symmetry EBSD detector. Data were collected at an accelerating voltage of 20 kV with beam currents in the range of 3–6 nA. Samples for corrosion testing in as-received and exposed conditions were investigated using secondary electron (SE) and backscattered electron (BSE) imaging using a scanning electron microscope (ZEISS Gemini 460 SEM) equipped with energy-dispersive X-ray spectroscopy (EDS) that was used for line scans and elemental maps.

TEM specimens were prepared via focused ion beam (FIB) lift-out, producing lamellae roughly 15 µm in length and subsequently thinned to ~120 nm in the regions of interest. TEM studies were conducted on an extreme field emission gun (XFEG) Talos F200X S/TEM (Thermo Fisher Scientific), operated at 200 kV and equipped with four detectors, which were used for elemental mapping using energy-dispersive X-ray spectroscopy (Bruker Super-X EDS). Mapping was performed at a probe current of ~1 nA with a sub-nanometer probe size and automatic drift correction every 30 s. Spectrum images were recorded on 1024 pixel grids, applying a 3 × 3 neighborhood filter during post-processing to improve signal quality. Typical acquisition times for each map ranged from 45 to 90 minutes.

TEM specimen thickness measurements were made using the convergent beam electron diffraction (CBED) method using a Spectra 300 S/TEM (Thermo Fisher Scientific) operated at 200 kV. CBED patterns were collected in a two-beam condition from various grains in the sample including g=<002>, g=<113>, and g=<224> type reflections, with the convergence semi-angle varied between 3 to 8 mrad to ensure the presence of the requisite three thickness fringes within each diffracted disk. The reciprocal distance between each fringe was measured to determine the corresponding excitation errors and then fitted to determine the sample thickness and extinction distance. The extinction distances calculated from linear regression were compared to theoretical values calculated for pure Ni as a reference face centered cubic material to ensure correct indexing of the first thickness fringe and an accurate thickness measurement.

2.5 ION IRRADIATION OF NAFA ALLOYS

NAFA-2 samples were irradiated to a target mid-range dose of 10 dpa with 11 MeV Cu^{3+} ions at temperatures of 300°C and 550°C at the Tennessee Ion Beam Materials Laboratory located at the University of Tennessee, Knoxville. Prior to irradiation, the NAFA-2 samples were subjected to a pre-irradiation annealing heat treatment of 1000°C for 1 h to simulate a pre-oxidation heat treatment. Then, the samples were sectioned such that the build direction was perpendicular to the direction of the ion beam with final sample thicknesses of approximately 1.6 mm. The samples were then mechanically polished using SiC grit papers, polycrystalline diamond suspensions, and a final 0.02 µm colloidal silica vibratory polish for 1 hour prior to the irradiation. Temperature control was accomplished using a K-type thermocouple welded to a 316 stainless steel dummy sample closely located next to the irradiated samples as shown in Figure 2. The beam was defocused and wobbled over a 6 mm by 5 mm irradiation area to achieve an even dose rate across the entire irradiated area, the shape and position of which are apparent in the right of Figure 2. The thermal history during the two irradiations as measured by the thermocouple is shown in Figure 3, which shows good thermal stability for the duration of both irradiations. The displacement damage and Cu implantation profiles were estimated using SRIM-2013 with the Kinchin–Pease model and are shown in Figure 4. The actual cumulative doses received during the two irradiations as calculated from beam current measurements were 10.1 and 11.8 dpa for the 300°C and 550°C irradiations respectively. The corresponding irradiation times were 9 hours and 16 minutes for the 300°C irradiation and 9 hours and 13 minutes for the 550°C irradiation. The beam current was also limited such that the corresponding mid-range dose rates were 3.0×10^{-4} dpa/s and 3.5×10^{-4} dpa/s for the 300°C and

550°C irradiations respectively. The chamber pressure was maintained below 1×10^{-7} Torr for the duration of both irradiations.

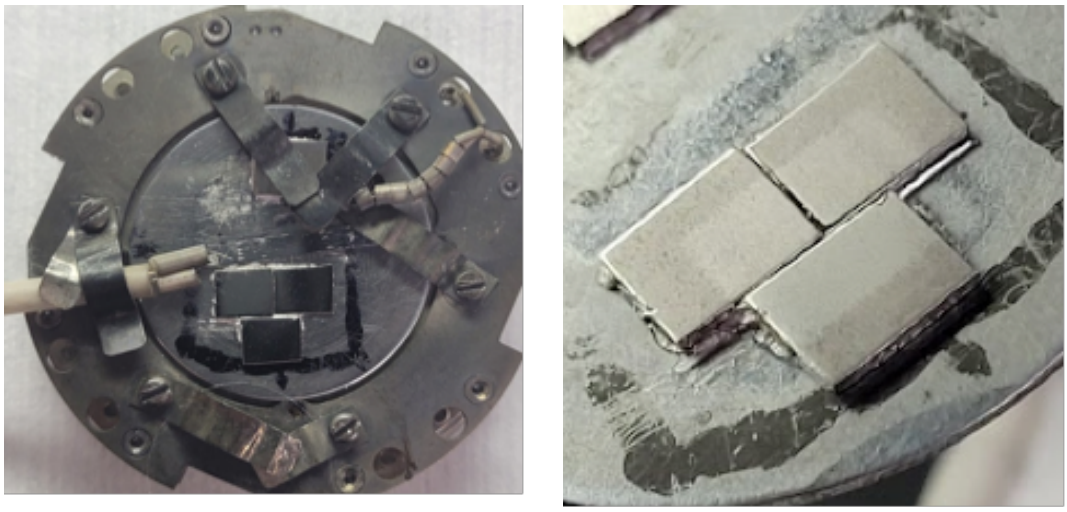

Figure 2. Ion irradiation stage setup for the 550°C irradiation. Three NAFA-2 samples mounted below a 316 stainless steel dummy sample with a spot-welded K-type thermocouple for temperature control (left) and the resulting 6 mm by 5 mm irradiated area after defocusing and wobbling the beam (right).

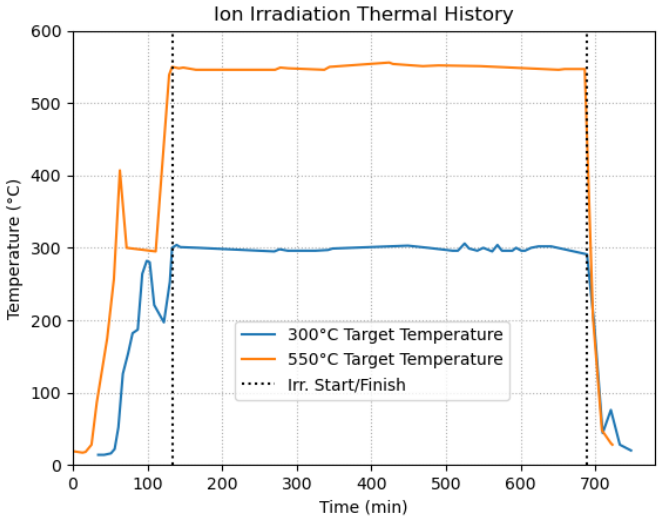

Figure 3. Temperature data for the ion irradiations collected via the K-type thermocouple welded to the 316 stainless steel dummy sample located closely next to the irradiated samples.

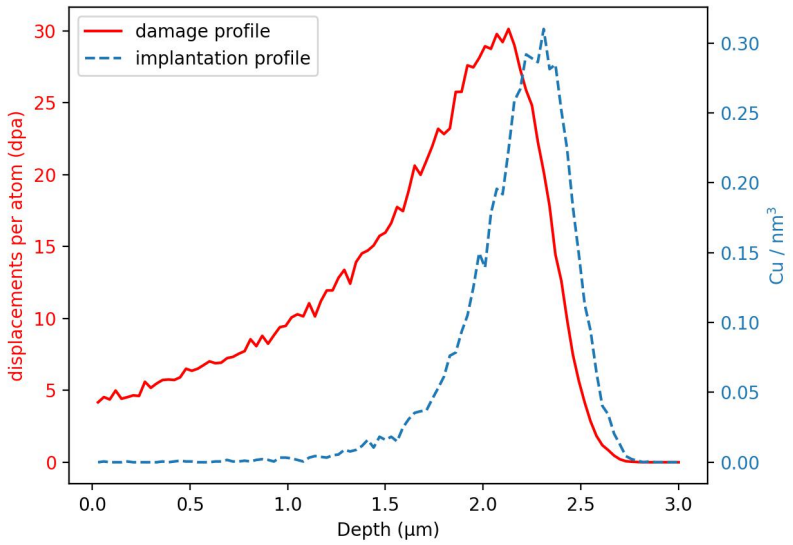

Figure 4. Ion irradiation damage and Cu ion implantation profiles as predicted using SRIM-2013 with the Kinchin-Pease model.

2.6 CORROSION TESTING PRE-OXIDATION, LIQUID NA EXPOSURES AND CHARACTERIZATION

After LPBF manufacturing according to conditions reported in Table 2 above, NAFA-1, NAFA-2, and cast NAFA-1 (measured compositions reported in Table 4) were EDM machined into subsized tensile specimens (SSJ geometry with thicknesses of 0.5 mm and/or 0.75 mm, respectively, depending on material heat) and milled to remove the residual EDM layer. LPBF NAFA-1 and NAFA-2 were machined along the build direction, whereas cast NAFA-1 was machined perpendicular to the build direction. Prior to machining, NAFA-2 was heat treated in an inert Ar atmosphere for 1 h at 1000°C, whereas NAFA-1 specimens were used in as-fabricated or as-cast condition.

Table 4. Measured powder compositions for LPBF NAFA-1 and NAFA-2 and measured alloy composition for Cast NAFA-1.

Composition (wt.%)	LPBF NAFA-1	Cast NAFA-1	LPBF NAFA-2 (heat: PC-11)
Fe	Bal.	Bal.	Bal.
Ni	22.71	22.3	25.3
Cr	17.3	17.05	15.17
Al	4.38	4	3.58
Mn	1.74	1.93	0.25
Si	0.45	0.5	0.2
Mo	1.07	0.99	1.98
Nb	0.72	0.59	1.37
N	0.03	5 wppm	280 wppm
C	0.52	0.48	<10 wppm
O	<0.01	*	270 wppm
Zr	0.12	0.09	0.21
Y	0.02	0.04	0.13
W	0.49	0.53	0.004

*Not measured

According to thermodynamic calculations at 700°C using the TCFE11 database, the following phases are expected for all studied alloys (Table 5). The calculation does not reflect prior 1 h heat treatment at 1,000°C in inert atmosphere.

Table 5. Studied alloys predicted phases at equilibrium at 700°C using Thermo-Calc TCFE12 database and alloy compositions reported in Table 4.

NAFA-1	NAFA-2
• FCC • Ordered β-NiAl • Al_2O_3 • MC (M= Nb, Zr) • $M_{23}C_6$ (M=Cr, Mo, Fe) • YAG phases	• FCC • Ordered β-NiAl • Disordered (Fe, Cr, Ni)Al • Laves phases • MC (M= Nb, Zr) • M_2O_3C (M=Y, Zr)

Subsized tensile specimens (SSJ geometry with thicknesses of 0.5 mm and/or 0.75 mm, respectively, depending on material heat) were EDM machined and milled to remove the residual EDM layer. LPBF NAFA-1 and NAFA-2 were machined along the build direction while cast NAFA-1 and cast AA253 were machined perpendicular to the build direction.

High-temperature liquid metal exposures were performed in Mo capsules (76.2 mm or 102 mm tall with a 25.4 mm outer diameter). A schematic of the corrosion setup and images of individual parts are reported in Figure 5. The capsules and caps were pre-cleaned with hydrofluoric acid and were inserted into the glove box. Specimens were exposed in individual capsules and attached to Mo end caps using Mo wires. The Mo capsules were then filled with 25 g of commercial sodium. Upon receipt, the commercial sodium was covered with oxides (99.0% metallic purity provided by Sigma Aldrich). The capsules were sealed by electron beam welding the end cap to the Mo capsule body in vacuum and gas tungsten arc welded in an argon-filled glove box (impurity levels ≤1 ppm O_2 and H_2O) to prevent the Mo from oxidizing during welding. As a safety measure, each capsule was sealed in an evacuated type 316 stainless steel outer capsule (Figure 5).

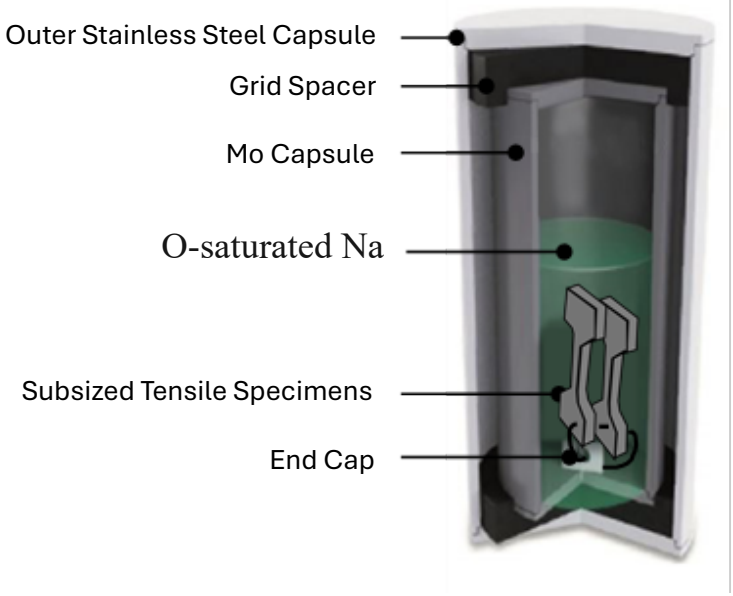

Figure 5. Schematic of SS-3 specimens in a Na-filled capsule.

Prior to liquid sodium exposures, some NAFA-1 and NAFA-2 specimens were subjected to a pre-oxidation treatment in air at 1,000°C in a box furnace without any gradual heating to avoid formation of transient oxides that typically occurs during the heating stage. Both bare and pre-oxidized specimens were exposed to O-saturated Na for 1,000 h at 700°C according to the test matrix reported in

Table 6 to study the stability of the formed Al_2O_3 layer in Na. Oxygen in Na was purposely not gettered using Zr foils to potentially minimize Na reduction of formed Al_2O_3 layer. To evaluate the impact of microstructure on Na compatibility an additional experiment was added with an as-cast coupon of NAFA-1 and was exposed for 1,000 h at 700°C in O-saturated Na shown in

Table 6.

Table 6. Summary of Na filled Mo capsules exposed for 1,000 h at 700°C

Capsule number	Specimens
1	2 bare SS3 LPBF-NAFA-1 type specimens
2	2 bare SS3 LPBF-NAFA-2 type specimens
3	2 pre-oxidized LPBF-NAFA-1
4	2 pre-oxidized LPBF-NAFA-2
5	1 coupon of bare Cast-NAFA-1

Specimens were weighed before and after air and Na environmental exposures using a Mettler Toledo XP205 balance with an accuracy of ±0.04 mg. After Na exposures, the samples were sequentially cleaned of residual Na using ammonia for environmental, health and safety concerns. The SSJ-3 specimens were tensile tested post-exposure at room temperature with an Instron 1125 machine per the American Society for Testing and Materials' ASTM E8-13 standard testing procedures at a strain rate of 0.015 min^{-1} controlled by crosshead displacement. Specimens were sectioned and mounted as cross sections and polished to 1 μm finish for microstructural characterization.

2.7 TENSILE TESTING

Uniaxial tensile testing was performed at room temperature and 600°C using the SS-J2 flat dog-bone as a test geometry (Figure 6). Gauge section width and thickness were measured in several locations along the gauge length using calipers, with the thinnest region of the gauge recorded for data analysis as it is where failure is most likely to occur. Specimens were loaded in a shoulder-loading style tensile fixture. In the case of elevated temperature testing, a 20 N preload was applied to offset thermal expansion during heat-up and maintain load train tension; specimen temperature was monitored directly via a thermocouple port machined into the back of the fixture near the specimen gauge section. Once the temperature was within ±5°C of nominal, a thermal soak of 5 minutes was initiated to ensure uniform temperature throughout the specimen. The specimen was then loaded until failure at a strain rate of 10^{-3}/s, or 5 μm/s, as measured by crosshead displacement; time, displacement, and load data were acquired at a rate of 10 Hz.

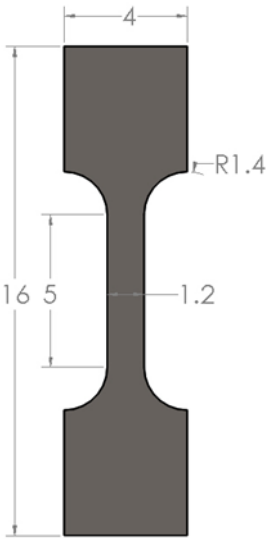

Figure 6. SS-J dog-bone tensile sample with nominal dimensions. Dimensions in millimeters, with thicknesses of 0.5 mm and 0.75 mm for SSJ-2 and SSJ-3, respectively.

As strain was not directly measured in this work, the elastic compliance of the load train must be factored out to ensure acceptable strain data quality. The load train or load-line compliance, C_{LL}, is defined as the inverse of the slope of the elastic region of the raw load-displacement curve. Plastic strain may then be calculated as:

$$\varepsilon_{p,i} = \frac{\delta_i - P_i C_{LL}}{L} \tag{3}$$

Where $\varepsilon_{p,i}$ is the plastic strain at data point i, δ_i and P_i are the corresponding raw displacement and load values, respectively, and L is the gauge length. Equation (3) is applied to all data points along the raw-load displacement curve, while load values are converted to engineering stress values. Points preceding the elastic limit are then truncated to create the stress-plastic strain curve, and the pertinent tensile values are extracted: the 0.2% offset yield stress (YS) is the engineering stress at 0.2% plastic strain, the ultimate tensile strength (UTS) is the maximum engineering stress, the uniform elongation (UE) is the plastic strain corresponding to the UTS, and the total elongation (TE) is the plastic strain at specimen failure.

2.8 FRACTURE TOUGHNESS TESTING

In addition to uniaxial tensile testing, fracture toughness testing was also performed, as it is essential for qualification of structural nuclear materials. The MBS-1 subsize three-point bend specimen (Figure 7) was selected as the test geometry. Prior to quasi-static bend testing, each specimen was fatigue precracked; this step is critical for accurate representation of the real-world physical damage incurred by structural materials during service. Specimens were fatigue loaded in a 13 mm span three-point bend at 15 Hz and a load range of 50 N minimum to 600–625 N maximum. Given the very small specimen geometry, direct crack growth measurement via clip gauge or direct current potential drop was not feasible. Instead, the change in specimen peak displacement during precracking was correlated to the change in precrack length. For a desired total precrack length of approximately half the specimen thickness (machined starter notch + fatigue precrack), it was found that an increase in peak displacement of approximately 16 μm after an initial "break in" period of approximately 3,000 cycles correlated to a total precrack length-to-thickness ratio of approximately 0.5. Upon reaching this threshold, the primary precracking step was terminated and a secondary precracking step was initiated, where the maximum load

was reduced such that the load amplitude was halved, and an additional 10,000 cycles were applied; this secondary step ensures a very sharp crack tip and therefore a very high stress concentration during monotonic testing. After this secondary precracking step was complete, the specimen was removed from the test frame and stored for later monotonic testing.

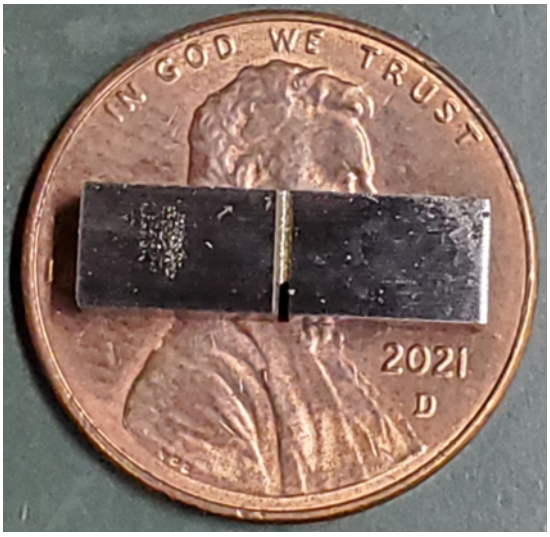

Figure 7. Notched MBS-1 three-point bend specimen with U.S. penny for scale. Nominal dimensions are 14.8 mm length, 4.5 mm thickness, 3 mm width. Starter notch aids in fatigue precrack initiation, and side grooves guide crack propagation direction and enhance the plane-strain condition.

Monotonic fracture testing was performed in air by reinstalling the specimen in the 13 mm three-point bend. In the case of elevated temperature testing (600°C), prior to testing a 20 N preload was applied to maintain tension to offset the thermal expansion of the load train. The temperature was then brought to ±5°C of the nominal temperature and allowed a 5-minute thermal soaking period before the test; specimen temperature was monitored directly via a thermocouple port machined into the back of the fixture. The specimen was then loaded in displacement control at 5 μm/s until either the load had dropped to half the maximum load of the raw load-displacement curve, or an excessive (~4.5–5 mm) displacement had been achieved. Time, displacement, and load data were recorded at 10 Hz. For room temperature tests, following testing the specimens were heat tinted in air at 450°C for 5–10 minutes to mark the final crack length. Finally, the specimen halves were separated manually.

In addition to load and displacement data, crack length data is also required for a complete fracture data set. The two fracture surfaces of each specimen were imaged under a low-magnification microscope to produce an image similar to Figure 8. In accordance with ASTM E1820 [12], nine evenly spaced points are measured at the initial and final monotonic crack fronts. The points at the side grooves are weighted by 0.5, and then all points are averaged (weighted average over 8); distances were measured in pixels and then converted to millimeters using the undeformed bottom edge of the sample as a reference scale. For this work, as both halves of each broken specimen were available, the initial and final crack lengths were averaged between the two halves for use in the data analysis.

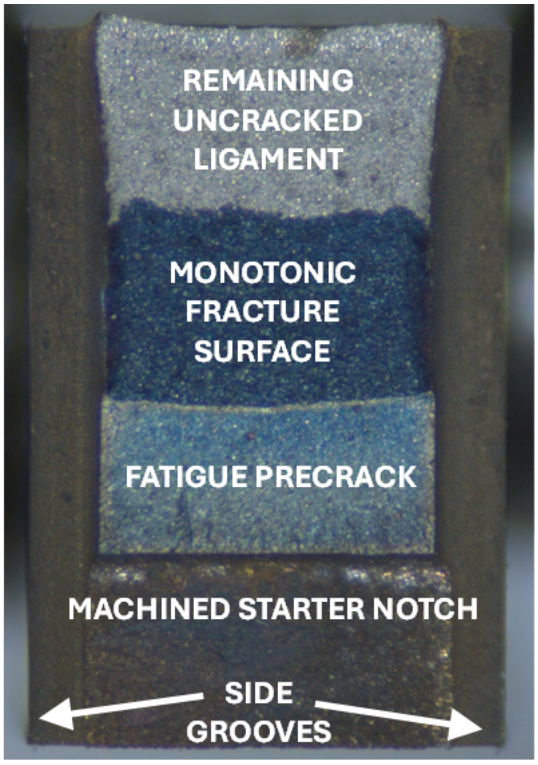

Figure 8. Fracture surface of MBS-1 specimen with key features identified.

With the load, displacement, and crack length data obtained, J-R fracture toughness is calculated using a slightly modified version of the curve normalization method in ASTM E1820, the modifications being (1) the flow stress is defined as the average of the yield and *true* ultimate tensile stress instead of the *engineering* tensile stress, and (2) the relationship between normalized displacement and normalized load in the crack propagation regime is assumed to be linear. As direct crack propagation cannot be measured due to the small specimen size and high elevated temperature, the curve normalization method is the only practicable method for calculating J-R fracture data. This method applies direct crosshead displacement data while factoring out the elastic compliance of the load train, analogous to tensile data processing where the elastic compliance of the load train is factored out to obtain plastic strain values. While not as accurate as direct measurements, such methodology is acceptable for the scope of this work.

After curve normalization analysis, the J-R curve is constructed, similar to the one featured in Figure 9. In addition to the J-R curve, the 0.2 mm offset line is also shown; this line has the same slope as the blunting regime of the J-R curve and an x-intercept of 0.2 mm. As materials that show stable crack propagation do not have a critical stress intensity factor K_{IC}, an interim stress intensity factor K_Q or K_{JQ} must be defined to simplify comparison between different materials and conditions. The K value corresponding to the 0.2 mm offset line is commonly reported as this interim value [13]:

$$K_{0.2mm} = \sqrt{\frac{EJ_{0.2mm}}{1-\nu^2}} \tag{4}$$

Where E is the elastic modulus, ν is Poisson's ratio, and $J_{0.2mm}$ is the J value of the J-R curve and 0.2 mm offset line intercept, analogous to the 0.2% strain offset used to define the yield stress in tensile data.

Equation (4) assumes the plane-strain condition is satisfied, though it is unclear for the materials explored in this work whether that condition is actually satisfied. The plane-strain condition is considered satisfied when the sample width is greater than ten times the radius of the plastic zone surrounding the crack tip [13]. Given that the toughness of these materials is significantly lower than those explored in [14], but that they do show some ductility, the issue of plane-strain satisfaction is ambiguous. Regardless, K_Q values are generally reported in accordance with Equation (4), as it is well-understood by nuclear-oriented fracture mechanists that subsize specimens often do not satisfy the plane-strain condition and that the viability of subsize-derived data as an engineering basis must be thoroughly scrutinized. Interim K_Q values are useful, however, for evaluating differences in fracture behavior between different materials and under different environmental conditions.

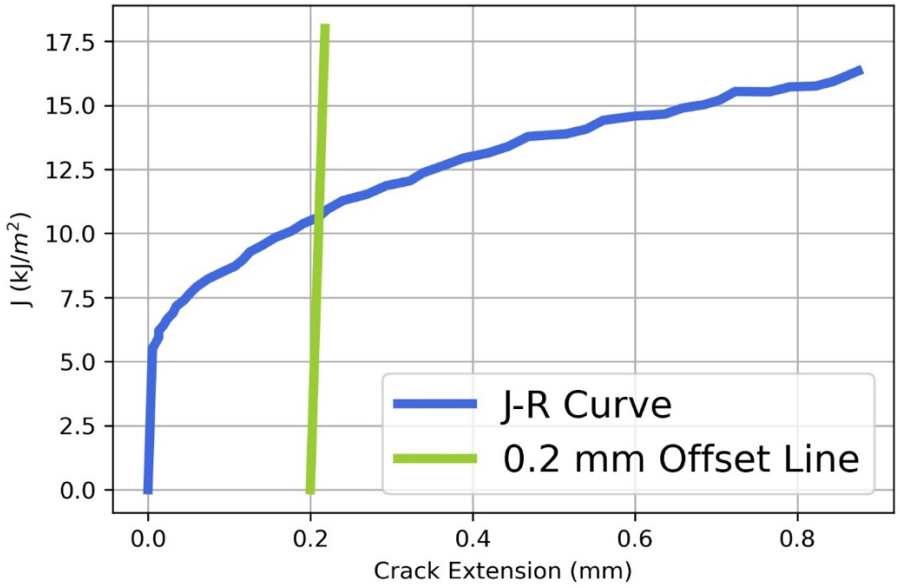

Figure 9. Example J-R curve with 0.2 mm offset line.

3. MICROSTRUCTURE AND MECHANICAL ANALYSIS

3.1 LPBF NAFA OPTIMIZATION

To address the cracking susceptibility of the baseline NAFA-2 alloy (AA241), four compositional variants were fabricated by arc melting and subsequently evaluated via constant-gas arc welding and oxidation testing. The primary design variables were the Nb, Cr, and Y contents. The baseline NAFA-2 alloy (AA241: 15 wt% Cr, 1.5 wt% Nb, +Y) exhibited extensive cracking in LPBF builds, associated with a pronounced eutectic microstructure and liquid film formation in the heat affected zone of the LPBF builds.

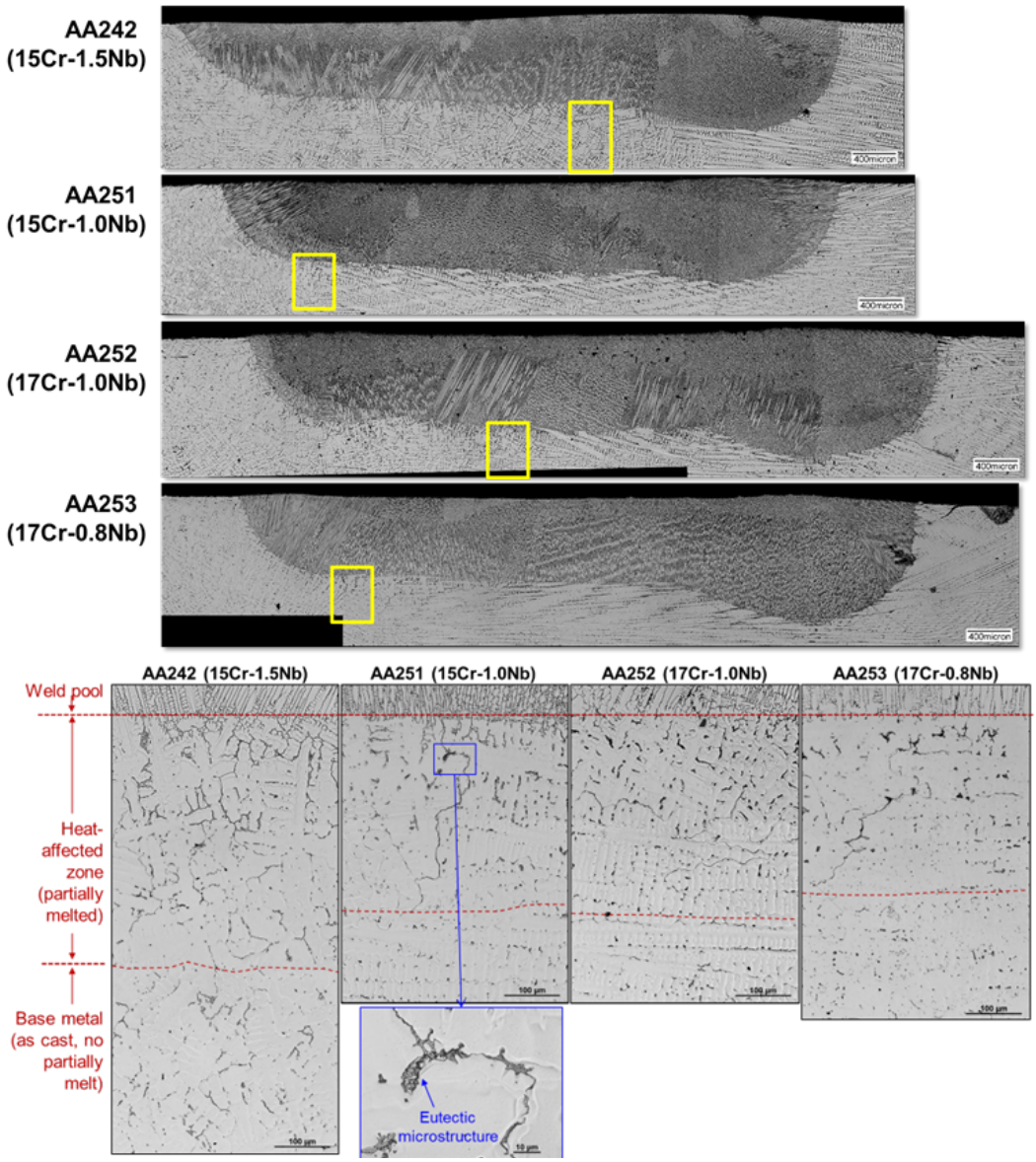

Figure 10. Microstructure of the four novel NAFA-2 alloy compositions mentioned in Table 3 at the top, with magnified areas marked in yellow highlighting the reduced eutectic microstructure formation with a decreased Nb amount.

Systematic variations with their microstructure shown in Figure 10 revealed that decreasing Nb content led to a reduced extent of eutectic solidification and a smaller HAZ. This effect was confirmed via SEM EDS examination, which found an increased amount of Nb within the microcracks. This effect is consistent with suppression of low-melting liquid film formation, which is believed to be the primary mechanism of crack initiation during solidification in LPBF. Increasing Cr was chosen to keep the expected good corrosion performance. All alloys were exposed to 1000°C oxidation in air for 2 h and 24 h. No significant changes were observed in oxide scale thickness or morphology across the variants, and the underlying microstructures remained unaffected by oxidation exposure. This suggests that modest variations in Nb and Cr within the tested ranges do not alter external oxidation resistance. An exception was noted for the baseline NAFA-2 alloy (AA241), which unexpectedly exhibited a transition toward internal oxidation/attack. The mechanism for this behavior remains under investigation.

Among the tested variants, the Cr-rich, low-Nb alloy (≈17 wt% Cr, 0.8 wt% Nb, without Y) provided the most favorable balance between printability and oxidation resistance, displaying reduced eutectic microstructure and improved solidification behavior. Although not sufficient on its own to eliminate cracking, conclusions regarding the impact of Nb and Cr could be drawn from this investigation. As NAFA-1 did not show cracking susceptibility, investigation efforts on the basis of the NAFA-1 chemical compositions were increased.

3.2 TEM ANALYSIS: DUAL PRECIPITATION COMPARISON BETWEEN NAFA-1 AND NAFA-2 AND ION-IRRADIATION RESULTS

TEM analysis of NAFA-1 and NAFA-2 was performed on materials produced via LPBF under Ar and N_2 atmospheres. As mentioned in Section 3.1, process optimization efforts for NAFA-1 were increased after the chemical composition of NAFA-2 has proven futile to produce a crack-free microstructure via LPBF printing.

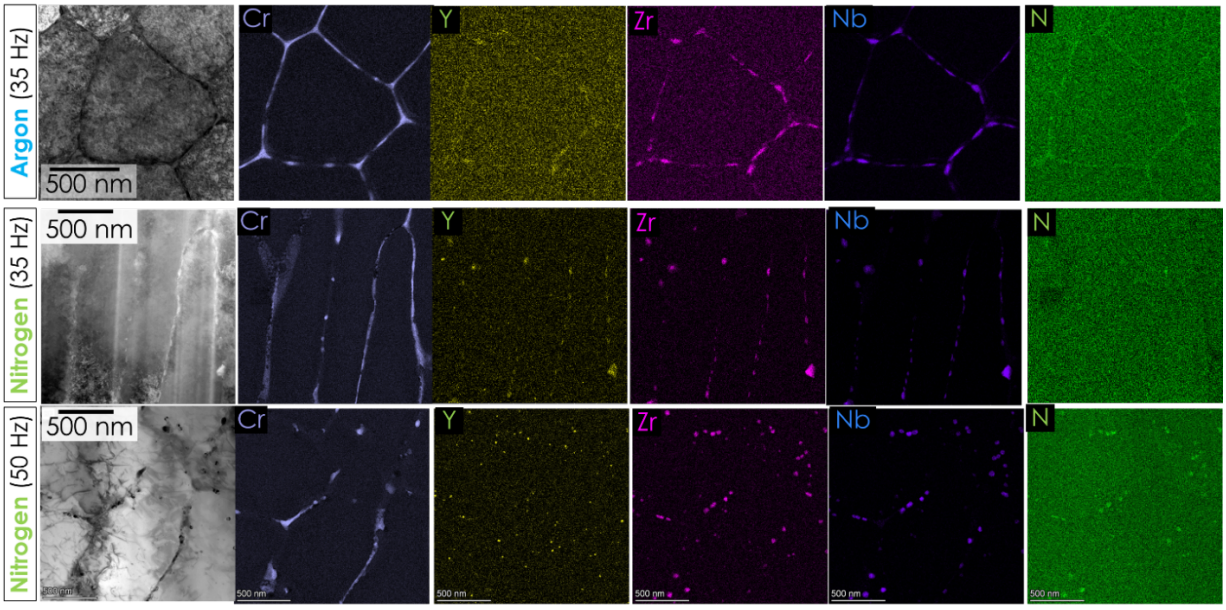

Figure 11. NAFA-1 printed under different process gas conditions, showing a clear separation of Y and Zr under a nitrogen printing environment.

Previously, printing with a gas mixture of Ar and N_2 with a low flow rate of 35 Hz displayed results similar to prints under a pure Ar atmosphere without any measurable significant differences. Those

findings led to the assumption that the gases spatially dissociate according to their atomic weight: Ar accumulates closer to the powder surface, whereas the lighter N_2 rises toward the ceiling of the printing chamber. Therefore, Ar was covering the powder surface for both prints resulting in similar microstructure and mechanical properties. For that reason, Figure 11 shows the original pure Ar print, in comparison to two prints in a pure nitrogen atmosphere with different flow rates of 35 and 50 Hz. Even though a higher magnification is used for the Ar prints in Figure 11, no small precipitates are visible outside the cell structure. In comparison, the same material printed under nitrogen atmosphere clearly shows the precipitate formation of small Zr-rich nitrides. A stronger co-alignment is visible for the nitrogen 35 Hz samples between Zr and Y, than for the 50 Hz sample, which indicates that a higher gas flow rate helps with a faster precipitation of Zr-rich nitrides and Y-rich oxides. That observation increased the chosen path for FY26 to move from LPBF to a directed energy beam system.

NAFA-2 printed under Ar gas was the material used for Cu ion-irradiation studies. To dissociate the ion-irradiation and the thermal annealing effect, the material was investigated side by side in an annealed condition (aged) and the Cu ion irradiated condition. The interest here is mostly in the impact of ion-irradiation on the stability of precipitates, as that determines the effectiveness of the precipitates as sinks for the trapping of gases. The STEM-EDS results of the aged and the ion-irradiated condition are shown in Figure 12Figure 12 and Figure 13, respectively.

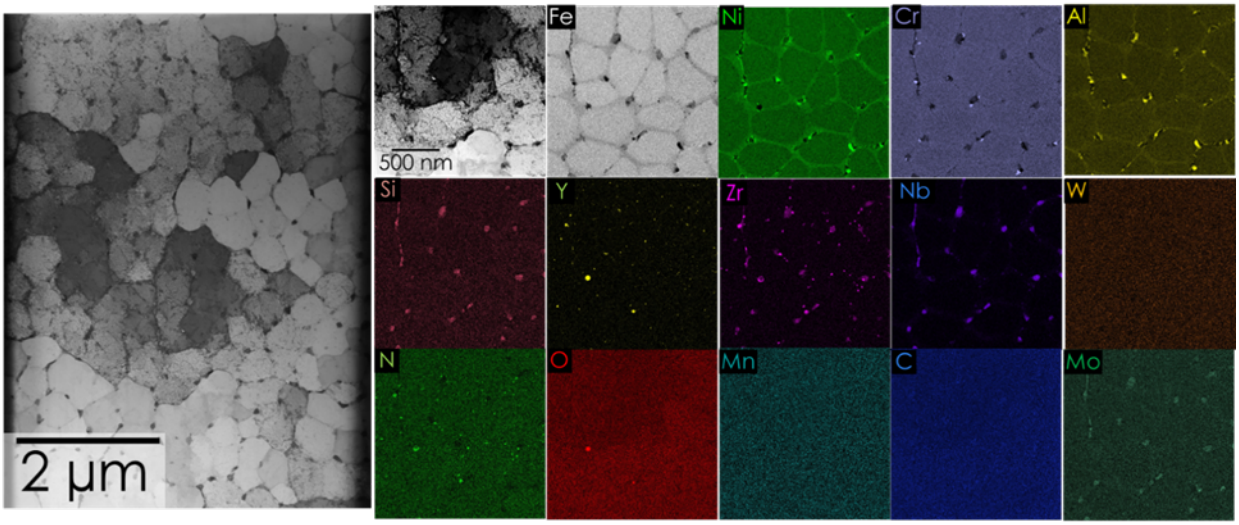

Figure 12. Aged NAFA-2 microstructure printed under Ar shows cell structure formation and a formation of oxides and nitrides.

A comparative study highlights that the impact of the ion-irradiation is most visible at the grain boundaries. Si and Nb are the dominant phases covering the grain boundaries in the irradiated condition. In the aged sample, Cr and Ni are segregated at the cell and grain boundaries, with Si and Zr located at triple points as smaller precipitates. No significant differences are identifiable for the Y-rich precipitates between the aged and the irradiated samples. The Zr-rich precipitates have changed significantly between the aged and the irradiated condition by being more co-aligned with Nb and the Si at the grain boundary. Zr-rich precipitates co-aligned in long stringers are not evaluated for the precipitate sizes because they do not contribute to an increased sink strength.

To achieve quantifiable results, TEM samples were investigated regarding the precipitate size and density. TEM lamella thicknesses were measured and the precipitate sizes, densities and co-alignment with each other are recorded for NAFA-2 and NAFA-1. The results are displayed in Table 7.

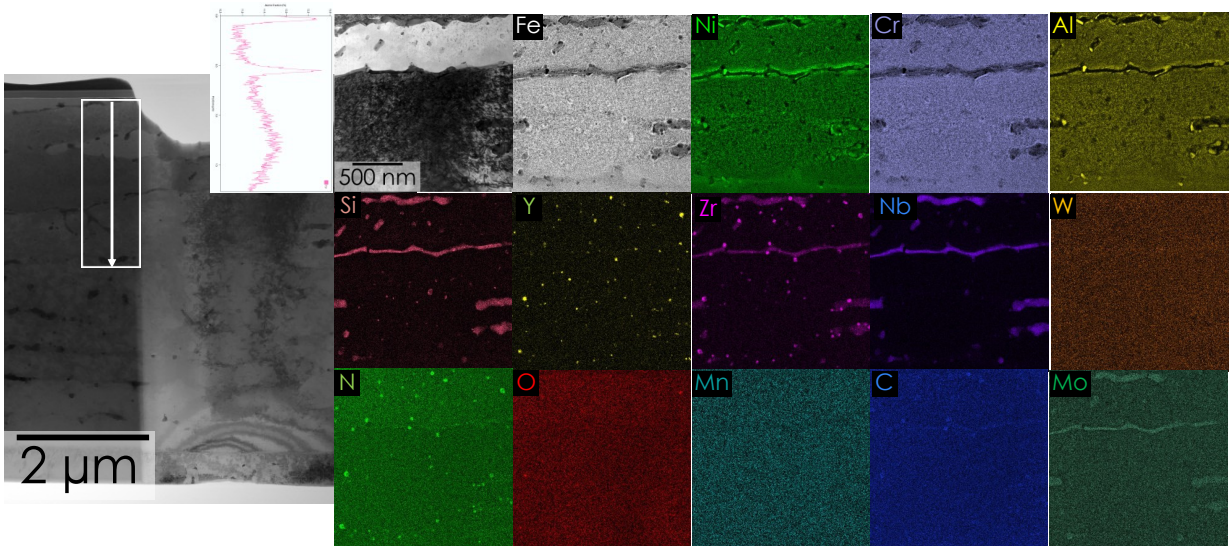

Figure 13. Cu Ion Irradiated NAFA-2 microstructure.

Table 7. Precipitate evaluation of NAFA-2 microstructure in various conditions, next to NAFA-1 printed under Ar and under N atmosphere.

	Set	Type	Equivalent circle diameter (nm)	Std.D (nm)	Median (nm)	Density in particles (m^{-3})	Volume fraction (%)	Co-aligned (%)
NAFA-2	N gas	Y	11.1	8.9	8.0	1.7×10^{21}	0.5	17
	N gas	Zr	15.4	3.4	14.9	9.0×10^{19}	0.3	64
	aged	Y	12.3	6.3	11.1	1.3×10^{21}	0.3	31
	aged	Zr	16.6	16.5	11.3	9.6×10^{20}	1.5	30
	Irrad	Y	14.2	8.9	11.1	9.6×10^{20}	0.4	30
	Irrad	Zr	19.0	15.1	11.6	5.7×10^{20}	0.7	42
	MA	Y	31.6	35.5	16.4	3.6×10^{20}	5.5	8
	MA	Zr	93.5	98.3	86.3	2.1×10^{19}	4.7	64
NAFA-1	Ar gas	Y	27.3	30.4	5.0	6.1×10^{19}	0.3	67
	Ar gas	Zr	34.6	26.8	42.9	2.1×10^{20}	1.3	22
	N gas	Y	14.3	11.5	9.3	9.9×10^{20}	0.5	45
	N gas	Zr	22.8	20.9	19.3	5.3×10^{20}	1.4	72

*Irrad: Cu ion irradiated; MA: Mechanically alloyed; Ar or N gas: Process gas during AM

To visualize the measured results from the table the equivalent circle mean diameter, median, co-alignment of precipitates, and density are plotted for yttrium- and for zirconium-rich precipitates in Figure 14 and Figure 15, respectively. These values together are most important to compare and increase the sink strength for the additively manufactured material and will guide the optimization strategy for the DED work, with the goal of maximizing the density, while minimizing the size and co-alignment. Precipitate growth is not significant from an irradiation perspective for both types of precipitates, but a small decline in precipitate density is visible with aging and irradiation for Y. The co-alignment changes slightly but remains within a margin of error. The density and volume fraction of Zr precipitates are highly dependent on the area and easily skewed by some large co-aligned precipitates with Nb.

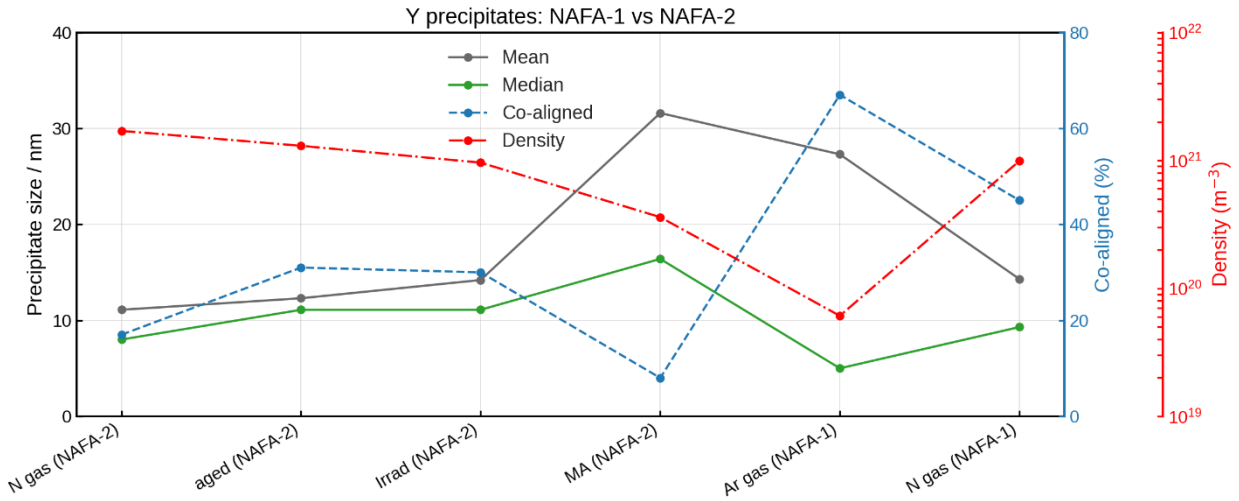

Figure 14. Yttrium precipitate comparison size and co-alignment with Zr precipitates in various conditions.

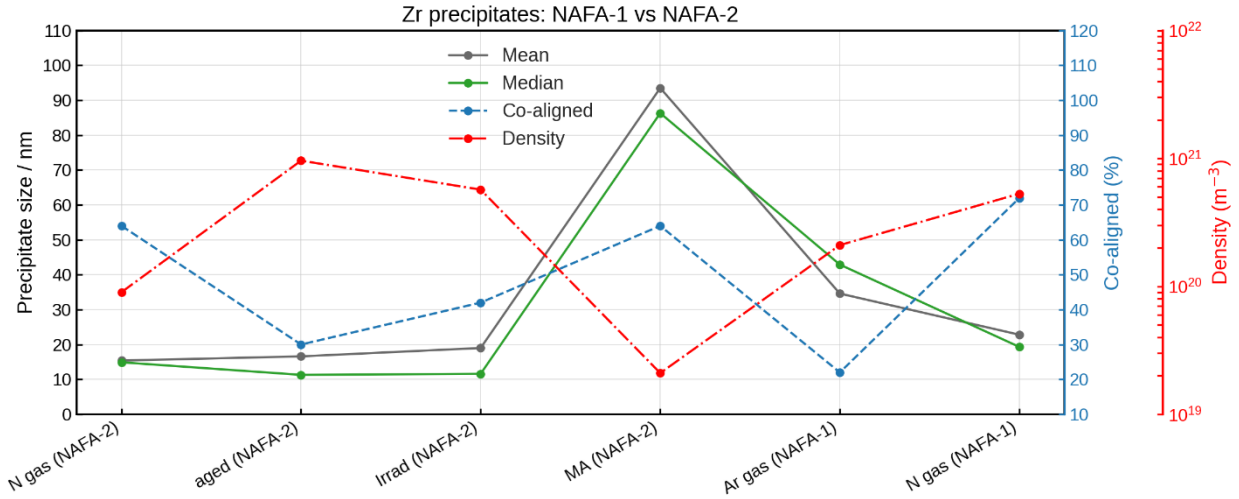

Figure 15. Zirconium precipitate comparison size and co-alignment with Y precipitates in various conditions.

A significant difference is found between the LPBF and the mechanically alloyed NAFA-2 samples. Here the microstructure proved more bimodal than in the AM LPBF samples. Larger precipitates and a much lower density of precipitates were found, but from detailed TEM analysis provided in the previous milestone report some areas are rich in precipitates, while others were void of precipitates. The results are used here in comparison with the statistical analysis with the LPBF data. Comparing the NAFA-1 prints

under Ar and under N atmosphere shows a clear trend to higher densities and smaller precipitates when a nitrogen atmosphere was used.

3.3 AS-PRINTED MECHANICAL PROPERTIES

The mechanical properties discussed here are focused on two primary conditions: (1) the as-printed properties of LPBF NAFA material in comparison with data previously generated on conventional AFA specimens and (2) the deterioration of the mechanical properties following Na exposures provided in the prior section.

First and foremost, the high strength of NAFA materials have been previously demonstrated, even in inert environments, in prior work published by this research team [15]. In this work, the evaluation of the mechanical properties of LPBF NAFA materials has been conducted after printing in both Ar and N_2 atmospheres, with tensile data shown in Figure 16 in comparison to the same material processed using conventional hot-isostatic pressing and conventional ball-mill and extrusion-based manufacturing processes (published previously in [11]).

From these curves, two points become evident. The first aspect is that the reactive atmosphere, although shown to influence the distribution of oxide and nitride nanoparticles in prior sections, has a negligible impact on the high-temperature strength of the LPBF NAFA material in comparison to the same print under inert atmosphere. This is not a significant issue, however, since both variants show a yield strength at room temperature that measures close to 800 MPa when tested in both the build direction and the transverse direction. The second outcome indicated by this figure is that conventional HIP and/or conventional ODS processing results in material with similarly high strength at room temperature, but with a significant drop in strength by 600°C. Similar to the high-temperature tensile results, the LPBF NAFA-1 material also exhibits double the resistance to crack propagation at these test temperatures (Figure 17). The enhanced ability of the LPBF NAFA material to retain its high-temperature strength and ductility at temperatures as high as 600°C in the as-printed form gives a strong argument for the use of net-shaped manufacturing processes like LPBF or DED to produce high-sink strength variants of advanced cladding materials.

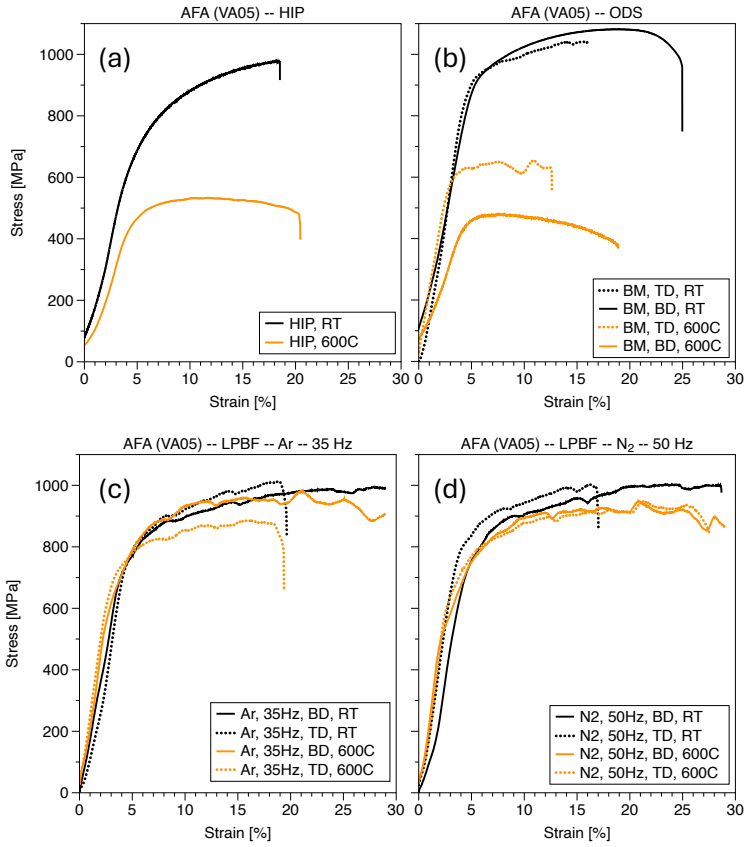

Figure 16. Engineering stress/strain curves generated at room temperature (black) and at 600°C (orange). Solid curves indicate specimens tested in the build direction and dotted curves indicate specimens tested in the transverse direction. HIP (a) and ODS (b) variants above have been previously reported in [11].

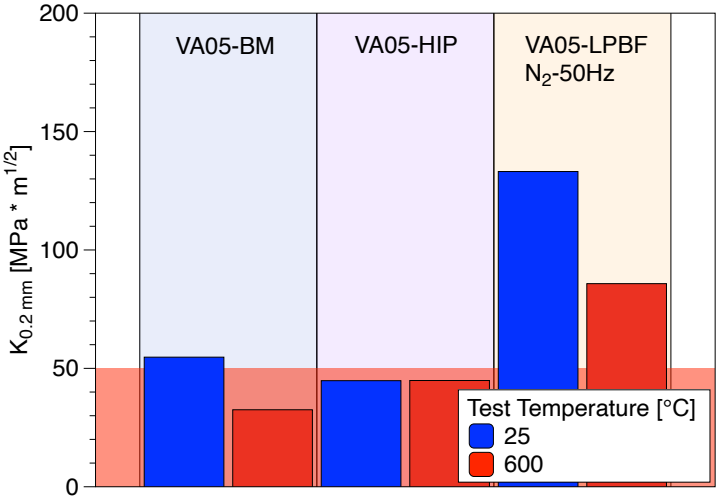

Figure 17. Comparison of room temperature (blue) and high-temperature (red) fracture toughness measurements of ODS (VA-05-BM), HIP (VA05-HIP), and LPBF (VA05-LPBF) variants of NAFA-1 versus a low-toughness criterion of 50 MPa·$m^{1/2}$ for suitability as a core structural material.

3.4 CORROSION TESTING

SEM and TEM cross section images and EDX elemental maps of NAFA-1 and NAFA-2 after 2 h pre-oxidation in air at 1,000°C are reported in Figure 18a and Figure 18b. After pre-oxidation, both alloys formed an Al-rich oxide layer, identified as Al_2O_3 using EDX point analyses.

In the case of NAFA-1, Cr-Mn and Ni-rich oxide nodules were locally formed on top of the Al_2O_3 layer (Figure 18a), whereas no oxide nodules formed on the Al_2O_3 layer of the NAFA-2 specimen (Figure 18b).

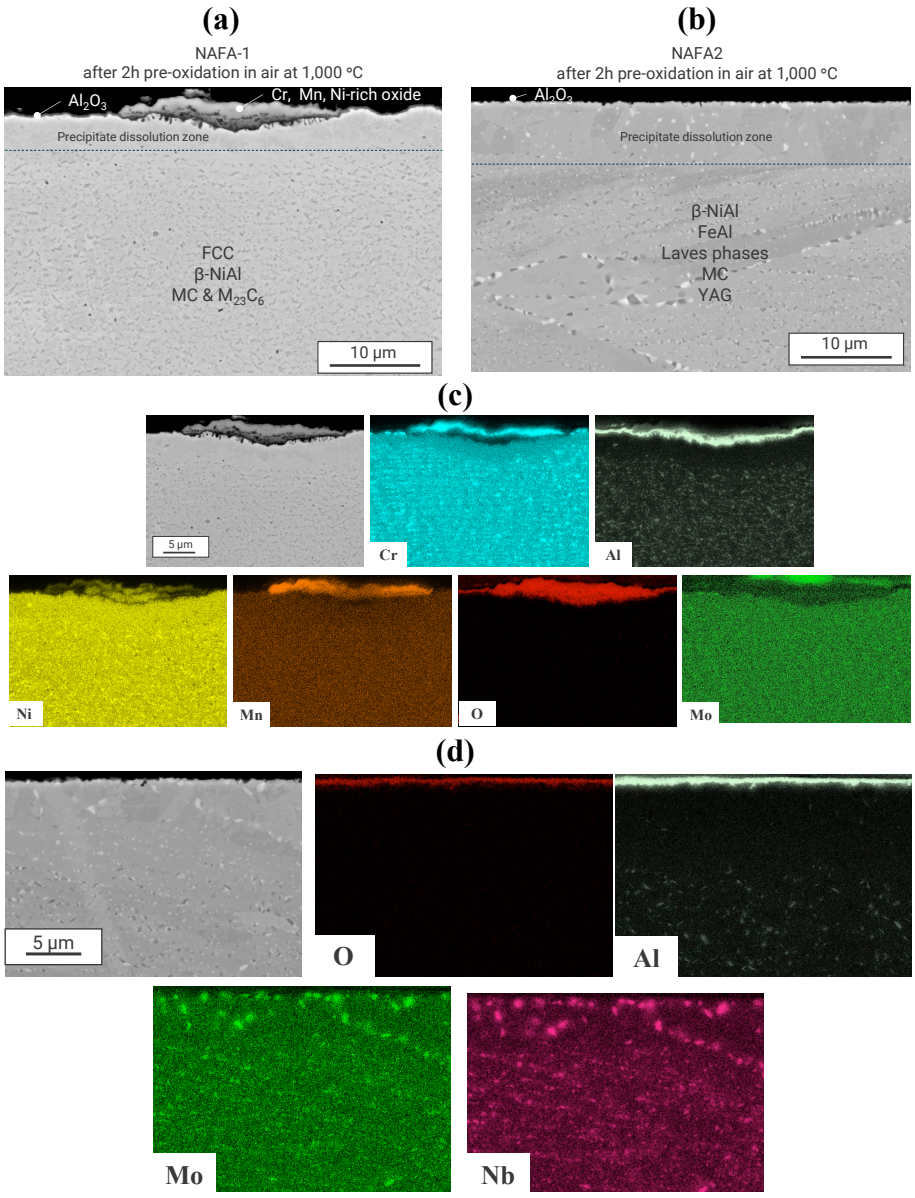

Figure 18. BSE images of (a) NAFA-1 and (b) NAFA-2 after 2 h pre-oxidation in air at 1,000°C with (c) and (d) showing their respective elemental mappings.

Underneath the oxide layers, a precipitate dissolution zone was observed (Figure 18a and b). The thickness of the precipitate dissolution zone varied between NAFA-1 and NAFA-2. In this zone Al-rich precipitates were dissolved in the case of NAFA-1 (Figure 18c). For NAFA-2 Al-rich precipitates were dissolved along with Mo-rich phases (most likely laves phases according to thermodynamic calculations) while Nb-rich precipitates remained mostly stable (Figure 18d). The stability of Nb-rich precipitates against oxidation induced dissolution was confirmed for NAFA-1 and NAFA-2 as well using TEM EDX elemental maps (not shown here). After 1,000 h in static oxygen saturated sodium at 700°C, mass changes were measured for bare and pre-oxidized LPBF, cast NAFA-1, and LPBF NAFA-2 specimens (Figure 19).

Large mass change variations were observed for both LPBF NAFA-1 and NAFA-2 (between −1 up to 5 $mg \cdot cm^{-2}$, as shown in Figure 19). Only one cast NAFA-1 specimen was tested, and mass gain was similar

to the average mass gain of LPBF NAFA-1 specimen. On average, mass gains were measured and much larger than average mass gains measured for bare 316H (0.10 ± 0.05 mg.cm-2) and bare C26M (0.15 ± 0.05 mg.cm-2) after 1,000 h in O-saturated Na at 700°C [16]. According to Figure 19, there is no apparent effect of pre-oxidizing treatment on mass change after O-saturated Na exposure.

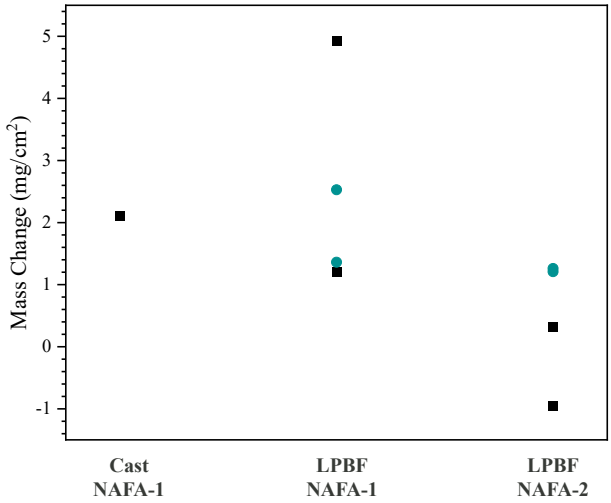

Figure 19. Specimen mass change measurements for bare Cast-NAFA-1 and bare (black) and pre-oxidized (blue) LPBF NAFA-1 and LPBF NAFA-2 and cast NAFA-1 after 1000 h in static O-saturated Na, Mo capsules.

3.4.1 Impact of Pre-Oxidation Treatment and Alloy Composition on Compatibility in O-Saturated Na

Figure 20 shows the BSE cross section images of bare and pre-oxidized LPBF NAFA-1. Depth of attack varied greatly between the pre-oxidized LPBF-NAFA-1 specimens in O-saturated Na (Figure 20a and b). Pre-oxidation treatment did not affect compatibility in O-saturated Na as depth of attack was similar for bare and pre-oxidized LPBF NAFA-1 specimens (Figure 20b and c). Depth of attack was also observed to vary for NAFA-2 bare specimens, and pre-oxidizing treatment did not affect compatibility with O-saturated Na.

Summarized depth of attack for bare and pre-oxidized LPBF NAFA-1 and NAFA-2 is reported in Figure 21, and the presence of oxygen in O-saturated Na governs the extent of attack to a larger extent than pre-oxidation treatment or alloy chemistry. It is unclear how these alloys would degrade in O-purified Na, which could be part of further investigation.

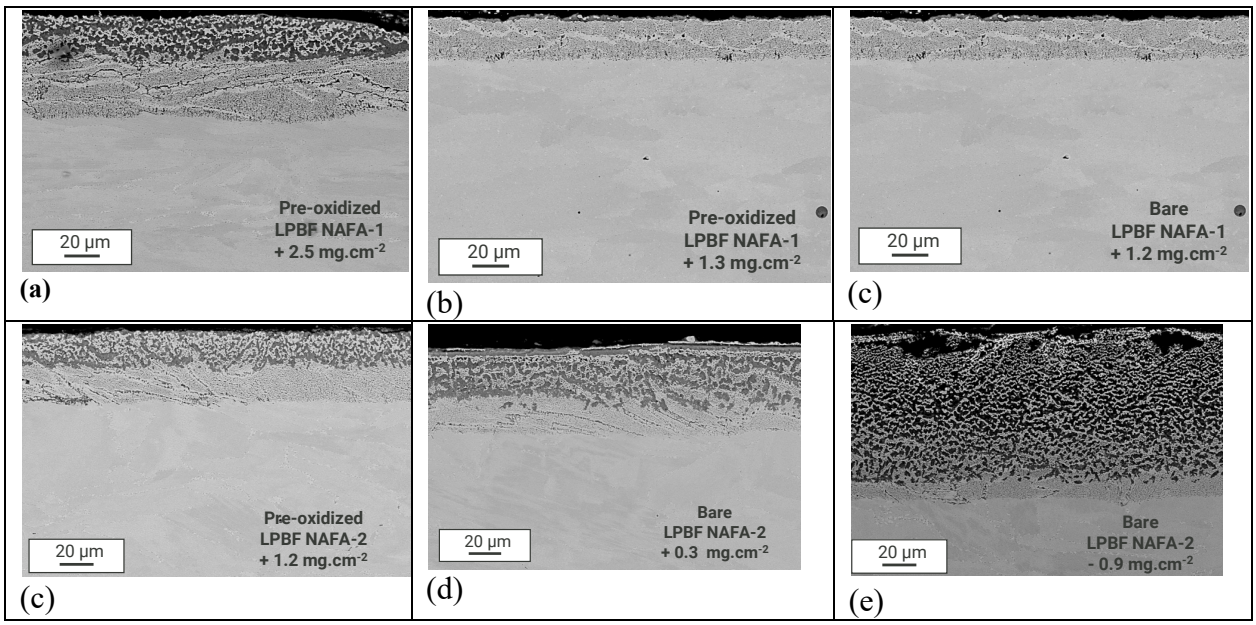

Figure 20. Bare and pre-oxidized LPBF NAFA-1 and NAFA-2 after 1,000 h in O-saturated Na at 700°C, Mo capsules.

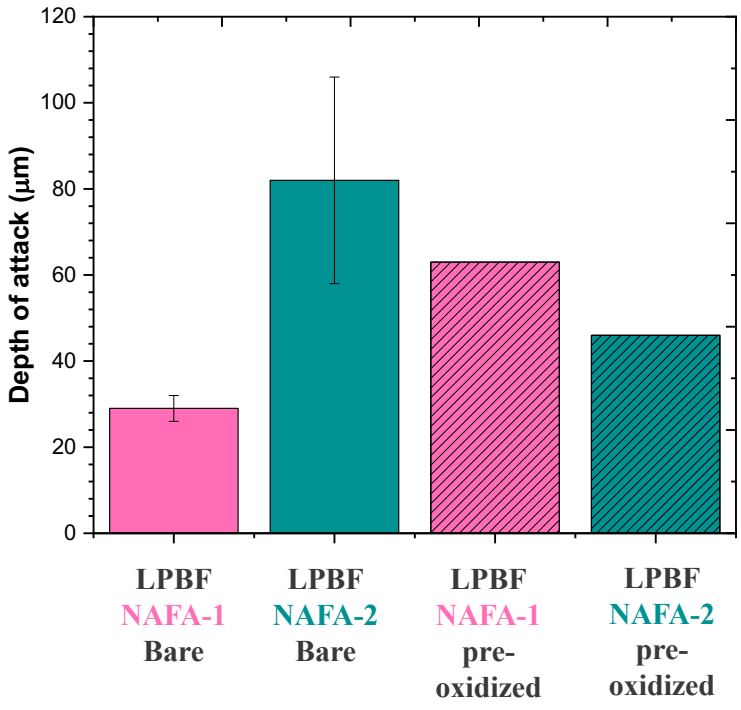

Figure 21. Summarized depth of attack determined using image analysis for bare and pre-oxidized LPBF NAFA-1 and NAFA-2.

3.4.2 Impact of Processing or Microstructure on Compatibility in O-Saturated Na

The impact of alloy microstructure was investigated by exposing bare cast NAFA-1 and bare LPBF NAFA-1 (Figure 22). Depth of attack was two times larger for cast NAFA-1 (64 ± 1 μm) than bare LPBF NAFA-1 (29 ± 3 μm) suggesting an impact of microstructure on compatibility in static O-saturated Na at 700°C. The cast NAFA-1 microstructure consists of larger grains and intergranular MC type carbides compared to LPBF fine grain structures and finely dispersed precipitates. The variation between LPBF and cast NAFA-1 is, however, of the same magnitude as the variation between bare NAFA-1 specimens, so it is unclear whether variations in sodium chemistry or microstructure is the result of the observed differences between cast and LPBF NAFA-1. Future experiments in O-saturated Na would help deconvolute these effects.

The nature of the corroded layer was analyzed using EDX elemental maps and line scans for bare cast and LPBF NAFA-1 after 1,000 h in static O-saturated Na at 700°C (Figure 23). In the case of bare LPBF NAFA-1, the corroded layer consisted of a discontinuous Cr-rich oxide layer overlaying Cr- and Al-rich internal oxides (Figure 23a) and the Cr- and Al-depleted zone (Figure 23a and Figure 24a). The corroded layer consisted of a larger Cr-rich internal oxidation zone and oxide precipitates and a larger Cr- and Al-depleted zone for bare cast NAFA-1 (Figure 23b and Figure 24b) compared to bare LPBF NAFA-1 (Figure 23a and Figure 24a).

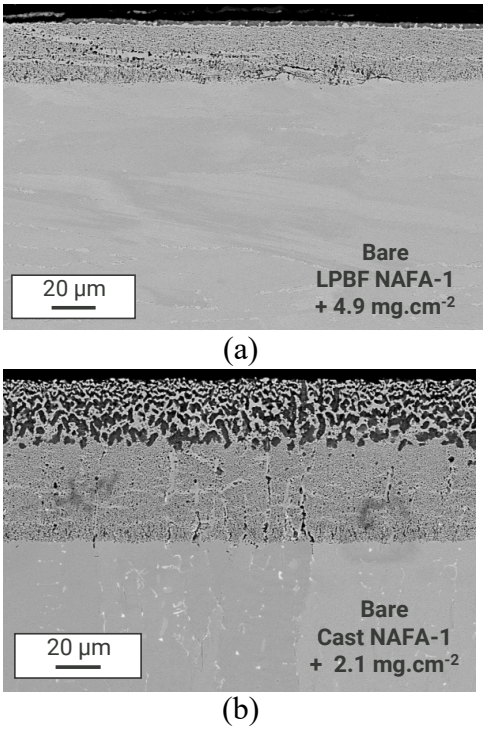

Figure 22. BSE cross section images of (a) bare LPBF NAFA-1 and (b) Bare Cast NAFA-1 after 1,000 h in static O-saturated Na at 700°C, Mo capsules.

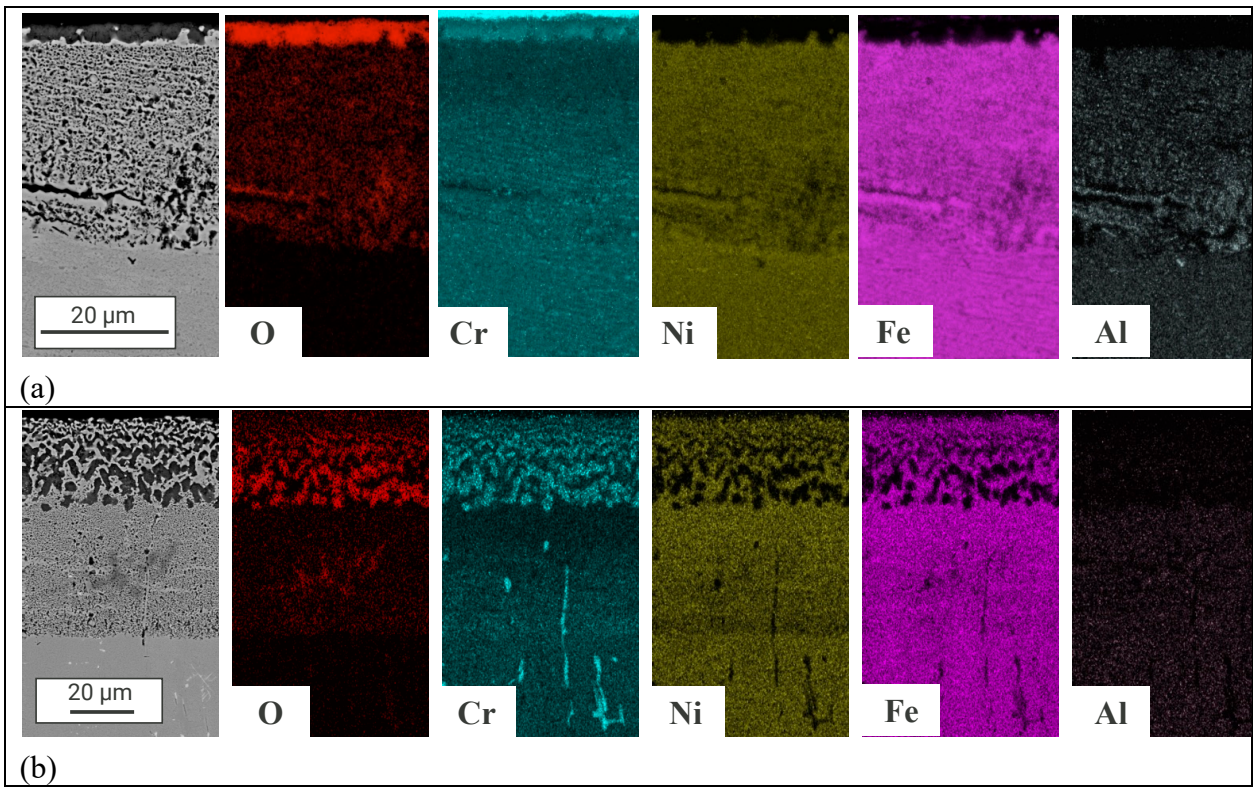

Figure 23. EDX quantified elemental maps of (a) bare LPBF NAFA-1 and (b) bare cast NAFA-1 after 1,000 h in static O-saturated Na at 700°C, Mo capsules. Note the scale bar difference between the two images.

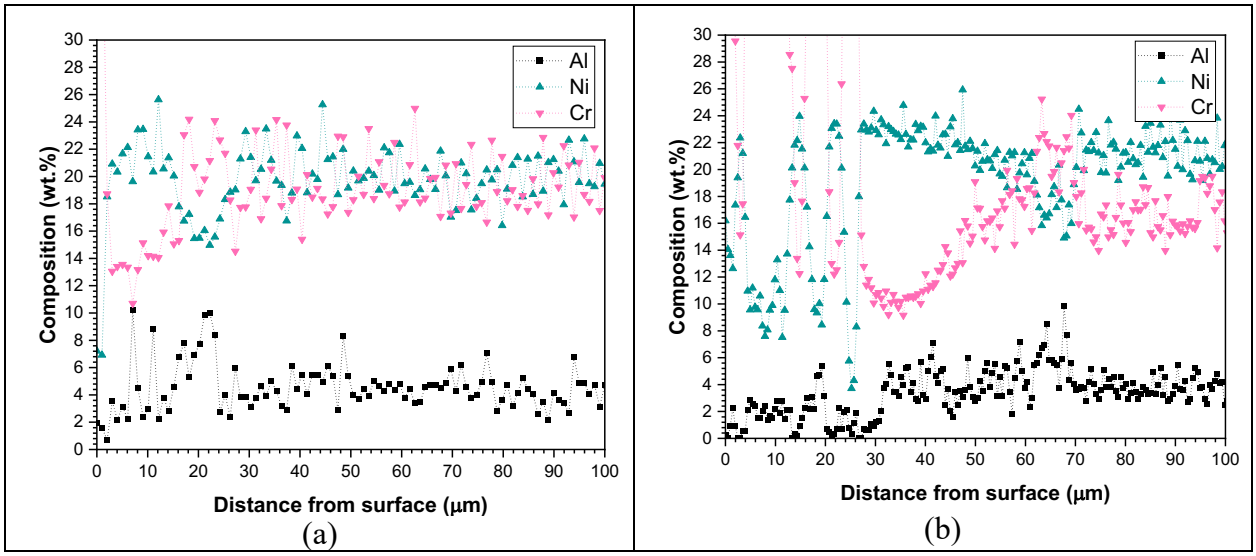

Figure 24. SEM EDX elemental line scans within (a) bare LPBF NAFA-1 and (b) bare cast NAFA-2 after 1,000 h in static O-saturated Na at 700°C, Mo capsules.

3.4.3 Stress-Corrosion Cracking in O-Saturated Na, Impact of Composition and Microstructure

After Na exposures, the SSJ-3 specimens were tensile tested at room temperature to evaluate the impact of the corroded layer on strength and ductility. Results are reported for bare and pre-oxidized NAFA-1 and NAFA-2 in Figure 25 before and after Na exposures. Stress-strain curves revealed no significant effect of corroded layer on ultimate tensile strength and ductility, but results varied between bare and pre-oxidized specimens suggesting an impact of Na and temperature combined on tensile behavior that will be reported in a future report.

However, the combined oxidized and dissolved layers on the surface of bare and pre-oxidized LPBF NAFA-1 and NAFA-2 affect susceptibility to cracking (Figure 26). Indeed, cracks were observed to form after tensile testing on the gauge section (Figure 26). In the case of bare LPBF NAFA-1, the crack length corresponded to the depth of the corroded layer (Figure 26 a) and in some cases propagated horizontally at the crack tip (Figure 26a). In the case of bare LPBF-NAFA 2, some cracks propagated beyond the depth of the corroded layer (Figure 26b), where it was located near defects or cracks within the LPBF NAFA-2 microstructure (Figure 26b) that were initially created during processing. It is unclear whether the presence of Na during mechanical testing will affect crack propagation, and this will be subject to FY26 investigations.

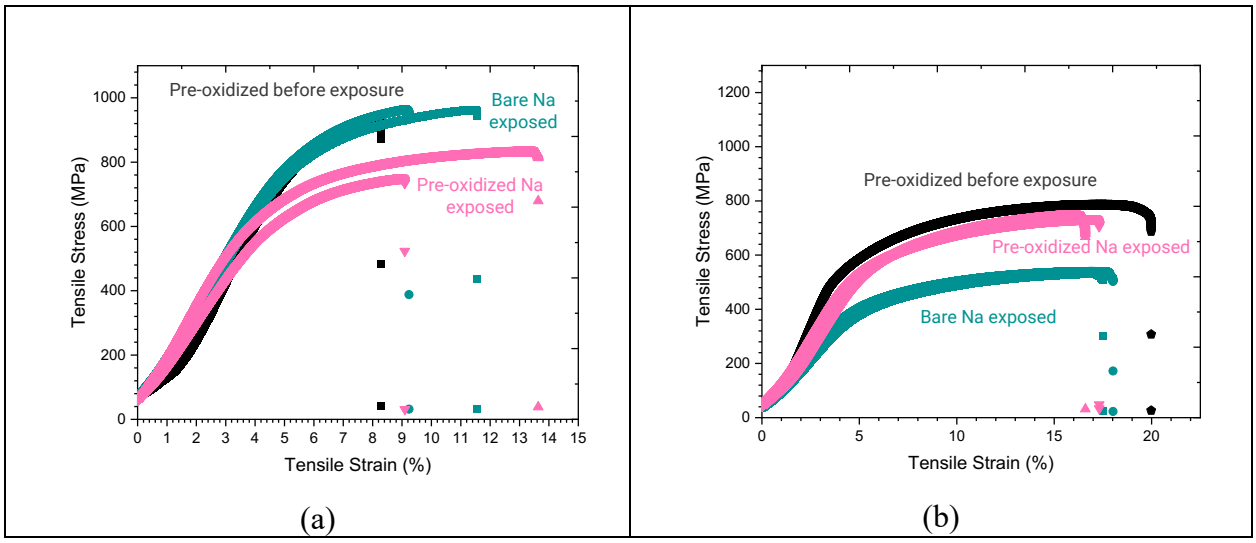

Figure 25. Stress-strain curve of (a) bare and pre-oxidized LPBF NAFA-1 and (b) bare and pre-oxidized LPBF NAFA-2 before and after 1,000 h in static O-saturated Na at 700°C, Mo capsules.

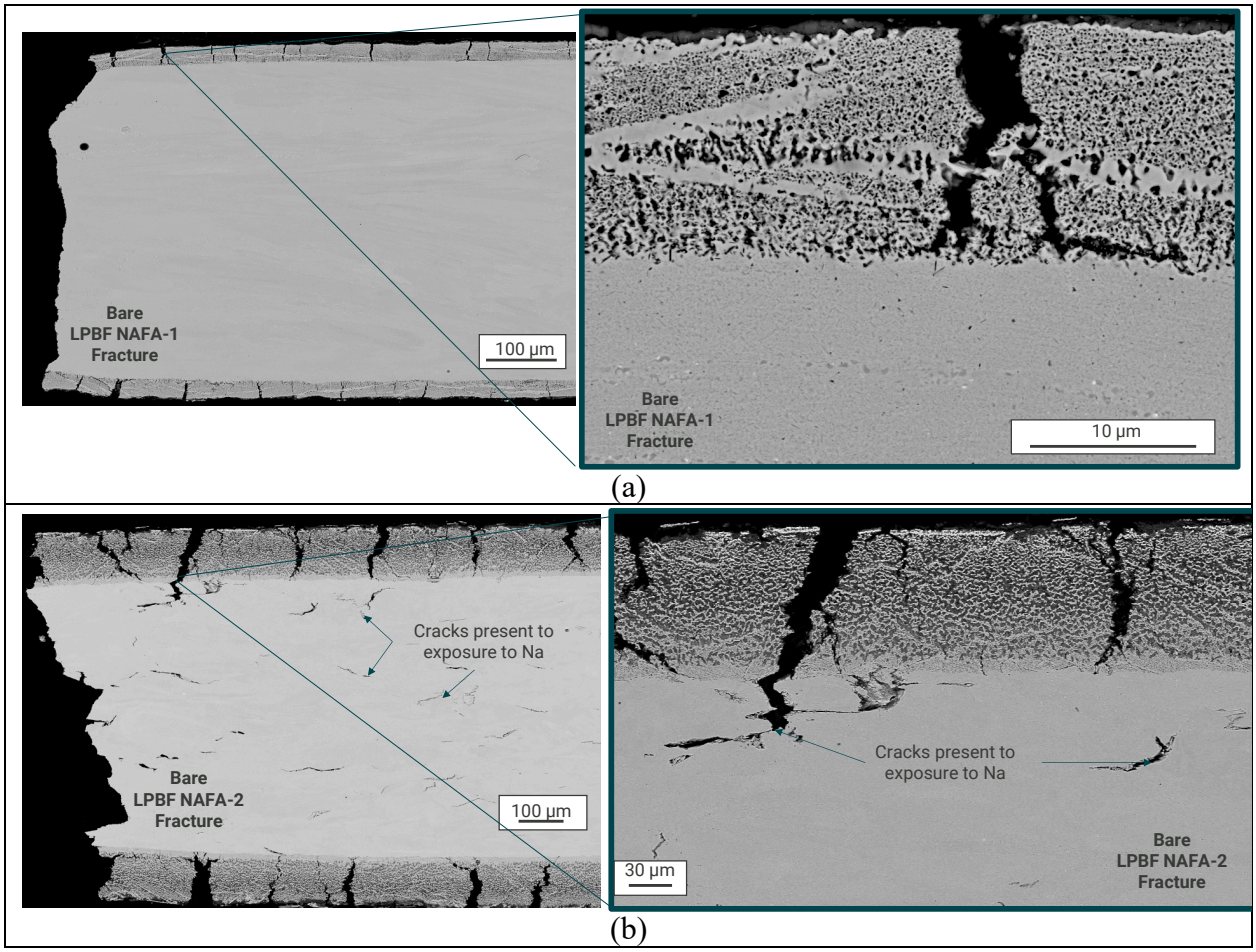

Figure 26. SEM-BSE images of (a) NAFA-1 and (b) NAFA-2 materials processed via LPBF following Na exposure and tensile testing.

3.5 FUTURE WORK

Our results demonstrate that the in situ formation during LPBF printing of nano oxide and nitride precipitates could produce high-sink strength variants of advanced cladding materials. While LPBF machines offer better surface finish compared to other AM systems, the production of ~6 feet long advanced cladding would require costly post-processing. The fabrication and subsequent pilgering of a smaller master tube could be considered, but this solution would not take full advantage of the near net shape capability of AM. Hybrid manufacturing, combining laser powder direct energy deposition (LP-DED) with subtractive machining in one platform, is likely a more efficient solution for advanced cladding production. LP-DED has already been evaluated for the fabrication of various advanced cladding candidate materials for advanced cladding such as RAFM steel[10-12] and ODS FeCrAl.[13] Printing of FeCrAl alloys under atmospheres containing oxygen was also performed to promote the formation of nano-oxides.[14] LP-DED printing in O_2 and N_2 rich environments is therefore a promising technique to produce advanced materials with a high density of nano oxides and nitrides. The use of a hybrid manufacturing platform ensures that precise machining of cladding measuring several feet long can be achieved while meeting the cladding geometric tolerance. Optimization of the parameters during both the deposition and machining steps will allow for control of the microstructure and residual stress.[15] Printing will be performed on very thin tubes selected for their formability and compatibility with nuclear fuels. This hybrid manufacturing approach is a very promising route to produce high-sink strength advanced LP-DED RAFM or LP-DED NAFA claddings.

4. CONCLUSIONS

This fiscal year, ORNL has made significant progress in establishing a fundamental understanding of nanostructured alumina-forming alloys and their performance under varied processing conditions. We were able to perform four parallel investigatory efforts surrounding (1) the effect of reactive atmosphere on precipitation, (2) the impact of minor alloying elements on solidification cracking, (3) stability of the microstructure under ion irradiation, and (4) compatibility of two NAFA compositions in contact with high-T sodium. The following conclusions can be drawn from the work summarized herein:

- Reactive atmosphere fabrication of two different NAFA materials has demonstrated consistent dual-precipitate dispersions for enhanced sink strength.
- At least one of the two compositions investigated to date is fully dense, with Nb-rich intermetallic formation as the mechanism for solidification cracking in some NAFA variants.
- LPBF NAFA materials outperform conventionally produced variants in both high-T tensile and fracture toughness performance metrics.
- Preliminary characterization of ion-irradiated LPBF NAFA materials suggests improved irradiation resistance vs. conventional wrought austenitic alloys.
- Although the NAFA material produced in this work is relevant for high-T oxidation resistance, new compositional variants of NAFA would be needed for high-T Na compatibility.
- FY26 efforts will focus on scaling the reactive-atmosphere cladding production to lengths exceeding those achieved this FY through transitioning to direct net-shape DED cladding production. Additional capsule tests in purified Na of cast and LPBF NAFA-1 will be performed to deconvolute the effect of microstructure on Na-compatibility from combined Na and oxygen effects.

5. REFERENCES

[1] Y. Yamamoto, M.P. Brady, Z.P. Lu, P.J. Maziasz, C.T. Liu, B.A. Pint, K.L. More, H. Meyer, E.A. Payzant, Creep-resistant, Al2O3-forming austenitic stainless steels, Science 316(5823) (2007) 433-436.
[2] Z. Yu, Y.-R. Lin, M.J. Zachman, S.J. Zinkle, H. Xu, The role of stacking fault tetrahedra on void swelling in irradiated copper, Communications Materials 5(1) (2024).
[3] H. Schroeder, High temperature embrittlement of metals by helium, Radiation Effects 78(1-4) (1983) 297-314.
[4] T. Horn, C. Rock, D. Kaoumi, I. Anderson, E. White, T. Prost, J. Rieken, S. Saptarshi, R. Schoell, M. DeJong, Laser powder bed fusion additive manufacturing of oxide dispersion strengthened steel using gas atomized reaction synthesis powder, Materials & Design 216 (2022) 110574.
[5] L. Autones, P. Aubry, J. Ribis, H. Leguy, A. Legris, Y. de Carlan, Assessment of Ferritic ODS Steels Obtained by Laser Additive Manufacturing, Materials 16(6) (2023) 2397.
[6] S. Saptarshi, M. DeJong, C. Rock, I. Anderson, R. Napolitano, J. Forrester, S. Lapidus, D. Kaoumi, T. Horn, Laser Powder Bed Fusion of ODS 14YWT from Gas Atomization Reaction Synthesis Precursor Powders, JOM 74(9) (2022) 3303-3315.
[7] H. Jia, Z. Zhou, S. Li, A new strategy for additive manufacturing ODS steel using Y-containing gas atomized powder, Materials Characterization 187 (2022) 111876.
[8] T. Gräning, M. Rieth, J. Hoffmann, A. Möslang, Production, microstructure and mechanical properties of two different austenitic ODS steels, Journal of nuclear materials 487 (2017) 348-361.
[9] J. Chen, P. Jung, T. Rebac, F. Duval, T. Sauvage, Y. De Carlan, M. Barthe, Helium effects on creep properties of Fe–14CrWTi ODS steel at 650° C, Journal of Nuclear Materials 453(1-3) (2014) 253-258.
[10] P. Edmondson, C. Parish, Q. Li, M. Miller, Thermal stability of nanoscale helium bubbles in a 14YWT nanostructured ferritic alloy, Journal of nuclear materials 445(1-3) (2014) 84-90.
[11] T.G. Seibert, C. Massey, D.T. Hoelzer, Y. Yamamoto, S. Dryepondt, H. Hyer, S. Nayir, J. Kendall, Nanostructured Alumina Forming Austenitic Alloy (NAFA) Production Using Mechanical Alloying and High-Temperature Consolidation, Oak Ridge National Laboratory (ORNL), Oak Ridge, TN (United States), United States, 2024.
[12] E1820 − 25a: Standard Test Method for Measurement of Fracture Toughness, ASTM International, 2025, pp. 1-70.
[13] R.W. Hertzberg, R.P. Vinci, J.L. Hertzberg, Deformation and fracture mechanics of engineering materials, John Wiley & Sons, 2020.
[14] C. Massey, P. Nandwana, H. Hyer, S. Nayir, G. Kumari, J. Kendall, C. Joslin, D. Collins, T. Graening, A. Godfrey, A.M. Rossy, A. Ziabari, Process–Property–Performance Mapping of Additively Manufactured 316H Stainless Steel Components, Oak Ridge National Laboratory (ORNL), Oak Ridge, TN (United States), United States, 2024.
[15] H.C. Hyer, S. Dryepondt, Y.-F. Su, Y. Yamamoto, B.A. Pint, C.P. Massey, Strength stability at high temperatures for additively manufactured alumina forming austenitic alloy, Scripta Materialia 253 (2024).
[16] M. Romedenne, R. Pillai, B. Harris, B.A. Pint, Compatibility of Fe-Cr-Al and Fe-Cr-Al-Mo oxide dispersion strengthened steels with static liquid sodium at 700 °C, Journal of Nuclear Materials 569 (2022).